

# Waves and vortices in the inverse cascade regime of stratified turbulence with or without rotation

Corentin Herbert<sup>1,2,†</sup>, Raffaele Marino<sup>3,4,5</sup>, Duane Rosenberg<sup>6</sup>  
and Annick Pouquet<sup>2,7</sup>

<sup>1</sup>Department of Physics of Complex Systems, Weizmann Institute of Science, 76100 Rehovot, Israel

<sup>2</sup>National Center for Atmospheric Research, P.O. Box 3000, Boulder, CO 80307, USA

<sup>3</sup>Laboratoire de Physique, ENS de Lyon, CNRS, Université de Lyon, F-69342 Lyon, France

<sup>4</sup>Laboratoire de Mécanique des Fluides et d'Acoustique, CNRS, Ecole Centrale de Lyon, Université de Lyon, F-69134 Ecully, France

<sup>5</sup>Dipartimento di Fisica, Università della Calabria, Ponte P. Bucci, cubo 31C, 87036 Rende, Italy

<sup>6</sup>National Center for Computational Sciences, Oak Ridge National Laboratory, P.O. Box 2008, Oak Ridge, TN 37831, USA

<sup>7</sup>Laboratory for Atmospheric and Space Physics, University of Colorado, Boulder, CO 80309, USA

(Received 31 July 2015; revised 22 July 2016; accepted 30 August 2016;  
first published online 30 September 2016)

We study the partition of energy between waves and vortices in stratified turbulence, with or without rotation, for a variety of parameters, focusing on the behaviour of the waves and vortices in the inverse cascade of energy towards the large scales. To this end, we use direct numerical simulations in a cubic box at a Reynolds number  $Re \approx 1000$ , with the ratio between the Brunt–Väisälä frequency  $N$  and the inertial frequency  $f$  varying from  $1/4$  to  $20$ , together with a purely stratified run. The Froude number, measuring the strength of the stratification, varies within the range  $0.02 \leq Fr \leq 0.32$ . We find that the inverse cascade is dominated by the slow quasi-geostrophic modes. Their energy spectra and fluxes exhibit characteristics of an inverse cascade, even though their energy is not conserved. Surprisingly, the slow vortices still dominate when the ratio  $N/f$  increases, also in the stratified case, although less and less so. However, when  $N/f$  increases, the inverse cascade of the slow modes becomes weaker and weaker, and it vanishes in the purely stratified case. We discuss how the disappearance of the inverse cascade of energy with increasing  $N/f$  can be interpreted in terms of the waves and vortices, and identify the main effects that can explain this transition based on both inviscid invariants arguments and viscous effects due to vertical shear.

**Key words:** internal waves, rotating turbulence, stratified turbulence

## 1. Introduction

The interaction between vortices and waves is a long-standing problem in fluid turbulence. It can lead to a self-sustaining process that is dominant, for example in

† Email address for correspondence: [corentin.herbert@weizmann.ac.il](mailto:corentin.herbert@weizmann.ac.il)

pipe flows, due to the strong wall-induced shear. A quasi-linear analysis around a mean but unsteady flow allows for a prediction of large-scale coherent structures in such flows (McKeon & Sharma 2010; Farrell & Ioannou 2012; Sharma & McKeon 2013), to the prediction of jets in baroclinic turbulence in the atmosphere of planets (Farrell & Ioannou 2009), and it can also be used as a tool to control the onset of turbulence using travelling waves (Moarref & Jovanović 2010). The dynamics of geophysical flows involves complex interactions between nonlinear eddies and waves due to the combination of planetary rotation and density stratification as well as the formation of shear layers. Typical parameters for the atmosphere and the ocean at large scales (larger than approximately 1000 km) are such that the dynamics of the fast waves is slaved to that of the eddies, and this leads to a quasi-geostrophic quasi-linear regime characterized by a balance between the pressure gradient and the Coriolis and gravity forces (Charney 1971). Then, the eddy turnover time is much larger than typical wave frequencies: the Brunt–Väisälä frequency  $N$  or the inertial frequency  $f = 2\Omega$  (with  $\Omega$  the rotation rate). For instance, frequency spectra obtained from *in situ* measurements in the ocean show distinct power laws for internal waves in the  $[f, N]$  band and geostrophic eddies at lower frequencies (Ferrari & Wunsch 2009). The quasi-geostrophic regime is well understood theoretically and provides a good description of the large scales of the atmosphere and the ocean (Vallis 2006, e.g.). However, the range of scales in these geophysical flows before dissipation prevails at small scales is such that other scale-dependent regimes can arise in which turbulence comes into play, with the eddy turnover time becoming comparable to the Brunt–Väisälä frequency, the inertial frequency, or their combinations which arise in the dispersion relation of internal waves. Lilly (1983), in particular, has underlined the emergence of a regime, coined stratified turbulence, between quasi-geostrophic turbulence and homogeneous isotropic turbulence (see also the scale analysis by Riley, Metcalfe & Weissman (1981)), and its importance for the mesoscales (with horizontal scales between 1 and 100 km, approximately) in the atmosphere. Indeed, the measured horizontal spectra of kinetic and potential energy in the upper troposphere and lower stratosphere (Nastrom, Gage & Jasperson 1984) has a long history of opposite interpretations: some have claimed that this unambiguous  $k^{-5/3}$  range corresponds to an inverse cascade of quasi-two-dimensional eddies (Gage 1979; Lilly 1983; Méttais *et al.* 1996), while others have argued that it was in fact a direct energy cascade dominated by internal waves (Dewan 1979), or yet another type of turbulence corresponding to a different scaling of the equations of motions (Lindborg 2006). This example emphasizes the importance of analysing data – be it observational, experimental or numerical – in terms of eddies or vortices on the one hand, and waves on the other hand. In this paper, we shall try to disentangle these two types of motion in the idealized context of direct numerical simulations of stratified flows with and without rotation in a periodic box, focusing on the classical quantities characterizing the statistical behaviour of nonlinear interactions in turbulent flows, in particular energy spectra and transfer functions. Our main goal is to better understand the fluid mechanics of rotating-stratified flows, motivated by geophysical flows. However, due to the computational difficulties in reaching geophysical flow parameter regimes (small Froude number and very large Reynolds number), we shall also discuss viscous effects which do not arise in geophysical flows, but are relevant for laboratory experiments such as those of Praud, Fincham & Sommeria (2005).

One way to distinguish between waves and eddies is through a decomposition of the flow onto the normal modes of the linearized system (Bartello 1995, see also below, § 3). Normal mode decomposition is a standard technique which has

been used in a variety of theoretical (Errico 1984; Warn 1986; Lien & Müller 1992; Bartello 1995; Waite & Bartello 2004; Herbert, Pouquet & Marino 2014) and numerical studies (Bartello 1995; Smith & Waleffe 2002; Waite & Bartello 2006*a,b*; Sukhatme & Smith 2008; Kitamura & Matsuda 2010; Kurien & Smith 2012; Brunner-Suzuki, Sundermeyer & Lelong 2014; Kurien & Smith 2014), for the Boussinesq equations, which we shall investigate here, as well as for other dynamical equations. Recently, another approach has been proposed (Bühler, Callies & Ferrari 2014), which relies on a few additional assumptions in order to be able to achieve a similar decomposition without a complete knowledge of the dynamical fields. This is particularly useful when working with observational data, such as ship track data or aeroplane measurements. Callies, Ferrari & Bühler (2014) have used this method to claim that observational data supported the internal wave interpretation of the forward cascade of the atmospheric mesoscales, although Lindborg (2015) argues using a similar technique that the forward cascade of energy could in fact be of another type, corresponding to the scaling regime of stratified turbulence identified in Billant & Chomaz (2001) (see also Lindborg 2006). Another interesting approach consists of computing a full frequency-wavenumber energy spectrum in the four-dimensional Fourier space (Clark di Leoni & Mininni (2015); see also Campagne *et al.* (2015) for an analogous analysis in a laboratory experiment of rotating flow). This allows one to directly assess how the energy is partitioned between modes which exhibit phase coherence, like waves, and other modes. However, this is a computationally expensive technique which requires a good time resolution in addition to a good space resolution (and hence, a lot of disk space).

In this context, a pioneering analytical and numerical study of strongly rotating-stratified turbulence in terms of normal modes was done by Bartello (1995). The link between geostrophic adjustment at large scale and the inverse cascade of energy due to the conservation of (linearized) potential vorticity is clearly established through a decoupling of the (fast) wave modes and vortical (slow) modes. By truncating the nonlinear interactions to some specific subsets of modes, as for example between three slow modes that lead to the inverse cascade of energy (Charney 1971), dominant effects can thus be identified. It is shown in particular that there are nonlinear interactions using a slow mode as a catalyst to push the wave energy to small scales (whereas triads involving three fast modes are negligible); furthermore, as the rotation is increased, the energetic exchanges between the slow vortical modes and the fast wave modes are weakened and such modes can be seen as actually being progressively decoupled. It was noticed by Smith & Waleffe (2002) that, for long times, the growth of large-scale energy is associated with geostrophic modes for  $1/2 \leq N/f \leq 2$  (in which domain three-wave resonances vanish completely), whereas for large  $N/f$ , the vertically sheared horizontal flows (VSHF), with no variation in the horizontal and no vertical velocity, are dominant. One should note that if the forcing wavenumber is not well separated from the box overall dimension, finite-size effects can develop that quench the possible (discrete) resonances, as already noted in the context of water-wave turbulence (see e.g. Kartashova, Nazarenko & Rudenko (2008) and references therein).

In the purely stratified case, it was found by Waite & Bartello (2004, 2006*b*) that the vertical spectrum of the waves moves to larger vertical wavenumber as stratification increases, in agreement with the argument found by Billant & Chomaz (2001) that the characteristic scale in the vertical is proportional to  $U/N$ , with  $U$  a typical large-scale velocity; at smaller scales the structures break down in a nonlinear fashion, although isotropy may not be restored, depending on the buoyancy

Reynolds number and whether the Ozmidov scale is resolved (see §2.2 below for definitions): the buoyancy scale  $L_B = U/N$  must be sufficiently resolved for overturning to take place. The case of comparable (but not identical) strengths for rotation and stratification was analysed by Sukhatme & Smith (2008), where it is shown that there is a transition in behaviour for  $N/f \approx 1$ : for smaller values, large scales are dominated by the vortical mode and small scales by wave modes, whereas for larger values of  $N/f$ , the wave modes dominate at all scales smaller than the forcing.

The scaling behaviour of slow and fast modes for rotating-stratified flows is analysed in Kurien & Smith (2012, 2014) for regimes where potential vorticity is linear, for small aspect ratio of the domain size in the vertical ( $\delta = L_{\parallel}/L_{\perp} = 1/4$ ), but with a unit Burger number  $Bu = \delta N/f$ , using high-resolution direct numerical simulations and hyper-viscosity. When compared to similar flows with  $\delta = 1$ , differences arise, as for example when examining the steepness of the wave component of the energy spectrum, viewed as a signature of the layered structure of the flow. The case  $\delta \neq 1$  was also examined for either purely rotating (Deusebio *et al.* 2014) or purely stratified flows (Sozza *et al.* 2015), where it is shown that the aspect ratio can affect the strength of the inverse cascade of energy to large scales. The combined effect of varying  $N/f$  and  $\delta$  on the formation of characteristic structures was further studied in Kurien & Smith (2014) for low Froude number ( $Fr = 0.002$ , ensuring that potential vorticity is again linear, i.e. for low effective turbulence) and varying either the Rossby number at fixed  $\delta$  or *vice versa* (in which case, the choice was made of  $N=f$ ). The layering of the flow is clearly dependent on the strength of the rotation ( $Fr$  being fixed), and the wave and slow mode spectra are quite different (when the total spectra are more difficult to distinguish). The inverse cascade of energy is clearly associated with the vortical (slow) mode, as shown as well in Brunner-Suzuki *et al.* (2014) for a variety of forcing functions in the context of sub-mesoscale oceanic mixing. It is also shown in Brunner-Suzuki *et al.* (2014) that small-scale (shear) layers do not directly modify the inverse cascade, although it could strengthen it when bringing together nearby vortices through nonlinear advection when they are sufficiently numerous. Recently, Whitehead & Wingate (2014) have studied the energy transfers between slow and fast modes in the Boussinesq equations, in the three asymptotic regimes of strong stratification/weak rotation, strong rotation/weak stratification and the quasi-geostrophic regime. Their findings also point out the role of the slow modes in the linear growth of kinetic energy.

Our study uses similar methods as the above-mentioned authors, but pursues a slightly different goal: here, we focus on the possibility of an inverse cascade and its relation with the inviscid invariants of the system. We are interested in understanding the difference between the rotating-stratified case, for which an inverse cascade is possible (Bartello 1995; Lindborg 2005; Aluie & Kurien 2011; Marino *et al.* 2013), and the purely stratified case, where there is no such thing (Waite & Bartello 2004, 2006b), although there is some transfer of energy towards the large scale. This difference has already been considered from the point of view of anisotropic energy transfers (Marino *et al.* 2014); here we adopt a different point of view and we investigate the role of vortices and waves in the inverse cascade (or lack thereof). We also aim at characterizing the transition between these two regimes. Indeed, although previous studies have established that, when an inverse cascade is present, it is due to the slow vortices, it is not clear how this phenomenology breaks up. We shall see that in the regime of parameters considered, we can identify three coexisting inertial mechanisms. To do so, we examine data stemming from direct numerical simulations of rotating-stratified turbulence, forced at small scales, for a variety of

$N/f$  ratios (and Froude and Rossby numbers) in cubic boxes at a Reynolds number of 1000. Since geophysically relevant buoyancy Reynolds numbers are currently out of reach for inverse cascade studies, the vertical shear associated with moderate buoyancy Reynolds numbers leads to potentially important viscous effects which we shall discuss in comparison to the inertial mechanisms. After describing the relevant equations, the theoretical framework and the numerical simulations in § 2, we review the normal mode decomposition in § 3, and analyse the numerical data in terms of the normal modes in § 4. Viscous effects and the role of the buoyancy Reynolds number are considered in § 5. In § 6, we discuss the results and present our conclusions.

## 2. Theoretical framework and numerical data

### 2.1. Equations of motion and direct numerical simulations

We consider incompressible flows in a reference frame rotating with angular velocity  $\Omega$  around axis  $\mathbf{e}_z$  (we note  $\mathbf{\Omega} = \Omega \mathbf{e}_z$  and  $f = 2\Omega$  the Coriolis parameter). The gravity field is anti-aligned with the direction of rotation:  $\mathbf{g} = -g\mathbf{e}_z$ . We work in the Boussinesq approximation: the density is assumed constant, equal to  $\rho_0 > 0$ , except in the buoyancy force term, and we assume a linear background stratification: the density field is given by  $\rho(\mathbf{x}) = \rho_0(1 - (N^2/g)z) + \rho'(\mathbf{x})$ , with  $N$  the Brunt–Väisälä frequency. Note that we are only considering the case of stably stratified flows. We introduce the temperature field (with the dimension of a velocity)  $\theta(\mathbf{x}) = (g/N\rho_0)\rho'(\mathbf{x})$ . The velocity field is denoted by  $\mathbf{u}$ . Given the assumptions mentioned above, the equations governing the dynamics of the fields  $\mathbf{u}, \theta$  are as follows:

$$\partial_t \mathbf{u} + \mathbf{u} \cdot \nabla \mathbf{u} = -\nabla P + \nu \Delta \mathbf{u} - 2\Omega \mathbf{e}_z \times \mathbf{u} - N\theta \mathbf{e}_z + \mathbf{F}, \quad (2.1)$$

$$\partial_t \theta + \mathbf{u} \cdot \nabla \theta = Nu_z + \kappa \Delta \theta, \quad (2.2)$$

$$\nabla \cdot \mathbf{u} = 0, \quad (2.3)$$

where  $P$  denotes the (rescaled) pressure field, fixed by the incompressibility condition,  $\nu$  the viscosity and  $\kappa$  the thermal diffusivity; we work with Prandtl number equal to unity:  $Pr = \nu/\kappa = 1$ . Finally,  $\mathbf{F}$  is an isotropic forcing introduced only in the momentum equation; it has a fixed amplitude in a prescribed narrow shell centred on wavenumber  $k_F$ , and random but constant in time phases. Note that, contrary to other studies (Kurien & Smith 2012, 2014, for instance), there is no forcing in the buoyancy equation, but the forcing has a vertical component (unlike, e.g. Waite & Bartello (2004) or Sozza *et al.* (2015)) and does not satisfy balance relations, even at the lowest order (unlike e.g. Waite & Bartello (2006*b*), where the forcing is only in the slow modes). The projection of the forcing on the waves and slow modes (see § 3) has the same magnitude; hence we are not favouring any of these modes *a priori*.

We integrate (2.1)–(2.3) numerically with a pseudo-spectral code, the geophysical high-order suite for turbulence (GHOST) in a tri-periodic cubic domain of length  $L = 2\pi$ . GHOST is parallelized using an hybrid MPI/OpenMP method and scales linearly up to  $10^5$  compute cores on grids of up to  $6144^3$  points (Mininni *et al.* 2011). No model is used for subgrid scales, and dissipation occurs through standard Laplacian terms. The runs considered here all have a resolution of  $512^3$ , with forcing at wavenumber  $k_F \in [22, 23]$ , and therefore Reynolds numbers  $Re \approx 10^3$ . The Rossby and Froude numbers vary as indicated in table 1; the runs can be grouped in two series, one with constant Froude number ( $Fr = 0.04$ ) and varying  $N/f$  (and therefore  $Ro$ ) and one with constant Rossby number ( $Ro = 0.08$ ) and varying  $N/f$  (and therefore  $Fr$ ). The isotropic energy spectra and fluxes of the above runs have already been analysed in Marino *et al.* (2013), providing evidence for the existence of an inverse cascade of energy in the presence of rotation and stratification, but not in the purely stratified case (see also Marino *et al.* 2014).

Id	$n_p$	$f$	$N$	$Fr$	$Ro$	$Bu$	$Re$	$\mathcal{R}_B$	$R_\omega$	$k_F$
R1/4	512 <sup>3</sup>	44	11	0.32	0.08	0.25	1000	102.4	2.53	22
R1/2	512 <sup>3</sup>	44	22	0.16	0.08	0.5	1000	25.6	2.53	22
R3/2	512 <sup>3</sup>	44	66	0.05	0.08	1.5	1000	2.5	2.53	22
R3	512 <sup>3</sup>	44	132	0.027	0.08	3	1000	0.73	2.53	22
R4	512 <sup>3</sup>	44	178	0.02	0.08	4	1000	0.4	2.53	22
F1/2	512 <sup>3</sup>	178	89	0.04	0.02	0.5	1000	1.6	0.63	22
F3/2	512 <sup>3</sup>	58	89	0.04	0.06	1.5	1000	1.6	1.90	22
F2	512 <sup>3</sup>	44	89	0.04	0.08	2	1000	1.6	2.53	22
F3	512 <sup>3</sup>	29	89	0.04	0.12	3	1000	1.6	3.80	22
F4	512 <sup>3</sup>	22	89	0.04	0.16	4	1000	1.6	5.06	22
F7	512 <sup>3</sup>	13	89	0.04	0.28	7	1000	1.6	8.85	22
F10	512 <sup>3</sup>	9	89	0.04	0.4	10	1000	1.6	12.65	22
F20	512 <sup>3</sup>	4.5	89	0.04	0.8	20	1000	1.6	25.3	22
F $\infty$	512 <sup>3</sup>	0	89	0.04	$\infty$	$\infty$	1000	1.6	$\infty$	22
F'20	512 <sup>3</sup>	4.5	89	0.04	0.8	20	2000	3.2	17.9	11
F' $\infty$	512 <sup>3</sup>	0	89	0.04	$\infty$	$\infty$	2000	3.2	$\infty$	11
F*20	1024 <sup>3</sup>	4.5	89	0.04	0.8	20	2000	3.2	17.9	22
F* $\infty$	1024 <sup>3</sup>	0	89	0.04	$\infty$	$\infty$	2000	3.2	$\infty$	22

TABLE 1. Model run parameters; names of runs at fixed Rossby number (respectively fixed Froude number) begin with a R (respectively F), followed by its  $N/f$  value.  $n_p$  is the number of grid points,  $N$  and  $f$  are the Brunt–Väisälä and the inertial frequency (with  $f = 2\Omega$ ,  $\Omega$  being the imposed rotation),  $Fr = U/[LN]$  and  $Ro = U/[Lf]$  are the Froude and Rossby numbers based on large-scale data, and the Burger number is defined as  $Bu = N/f$  for a cubic box as used here;  $\mathcal{R}_B = ReFr^2$  and  $R_\omega = Re^{1/2}Ro = \omega_{rms}/f$  are, respectively, the buoyancy Reynolds number and the micro-Rossby number, and  $k_F$  is the forcing wavenumber. The runs belonging to the no-resonance zone have a shaded background. The primed and starred runs in the last four lines are sensitivity tests with respect to the buoyancy Reynolds number, described in § 5.2.

## 2.2. Characteristic scales

Rotating-stratified turbulence covers a wide range of physical regimes, which can be characterized by three non-dimensional numbers, besides  $Pr$ . Given a characteristic length scale  $L$  and a characteristic velocity  $U$  at that scale, we introduce as usual the Reynolds number  $Re = UL/\nu$ , the Rossby number  $Ro = U/(fL)$  and the Froude number  $Fr = U/(NL)$ . The Rossby and Froude numbers quantify the strength of the Coriolis and buoyancy forces, respectively. They correspond to the ratio between a wave period ( $f^{-1}$  and  $N^{-1}$ , respectively) and the eddy turnover time  $L/U$ .

A difficulty in rotating-stratified flows arises from the variety of characteristic scales one can construct. To start with, the Froude number can be based on a characteristic horizontal length scale or a vertical length scale. It is known that stratified turbulence develops strong gradients in the vertical (leading to the ubiquitous layered structure of the flow, see e.g. Herring & Métais (1989)), in such a way that the vertical Froude number remains of order unity (Billant & Chomaz 2001; Lindborg 2006), even when the horizontal Froude number is small. The corresponding vertical length scale is the buoyancy scale,  $L_B = U/N$  and can be identified readily in such flows (see e.g. Rorai, Mininni & Pouquet 2014). In the presence of rotation, the layers are expected

to be slanted (with respect to the horizontal). In that case, it was conjectured that the characteristic length scale in the vertical also involves both  $N$  and  $f$ , like a deformation radius, for which the effects of rotation and stratification balance each other, with  $Nk_{\perp} \sim fk_{\parallel}$  (Charney 1971). It was shown by Rosenberg *et al.* (2015) that a Froude number based on a vertical Taylor scale involving vertical velocity gradients,  $\ell_z = \sqrt{\langle u_{\perp}^2 \rangle / \langle (\partial_z u_{\perp})^2 \rangle}$  (where the angular brackets denote spatial averaging) is also very close to unity. Here, we define the Froude and Rossby numbers (as well as the Reynolds number) based on the scale of the forcing,  $L_F = 2\pi/k_F$ . Since the forcing is isotropic, there is no reason to distinguish between vertical and horizontal Froude number with this definition, although anisotropies and different characteristic scales in the horizontal and the vertical will of course develop spontaneously in the flow. It follows that for the purpose of our study, at unit aspect ratio, the ratio of the Rossby and Froude numbers  $Bu = Ro/Fr$ , referred to as the Burger number, reduces to the ratio of the Brunt–Väisälä frequency and the Coriolis parameter:  $Bu = N/f$ . The characteristic velocity  $U$  used to evaluate the non-dimensional numbers is the rms velocity of the initial condition.

The recovery of isotropy should occur at a scale for which the eddy turnover time and the wave period become comparable. This allows one to define an Ozmidov and a Zeman scale (Zeman 1994; Mininni, Rosenberg & Pouquet 2012) written, respectively, for purely stratified or purely rotating flows, assuming an isotropic Kolmogorov range,  $E_V(k) \sim \epsilon_V^{2/3} k^{-5/3}$  at small scale, as:

$$\ell_{Oz} = \sqrt{\frac{\epsilon_V}{N^3}}, \quad \ell_{Ze} = \sqrt{\frac{\epsilon_V}{f^3}}, \tag{2.4a,b}$$

with  $\epsilon_V = \nu \langle \omega^2 \rangle$  the kinetic energy dissipation rate. The Froude and Rossby numbers measure the ratio of these scales to the characteristic scale:  $Fr = (\ell_{Oz}/L)^{2/3}$ ,  $Ro = (\ell_{Ze}/L)^{2/3}$ . Finally, if one wants to construct a measure of the actual development of small scales in the flow, a buoyancy Reynolds number  $\mathcal{R}_B$  and a micro-Rossby number  $R_{\omega}$  can be defined in the following way:

$$\mathcal{R}_B = Re Fr^2, \quad R_{\omega} = \frac{\omega_{rms}}{f} = Re^{1/2} Ro, \tag{2.5a,b}$$

so that  $R_{\omega}^2$  is the equivalent, for rotation, of the buoyancy Reynolds number. The buoyancy Reynolds number  $\mathcal{R}_B$  corresponds to the ratio of vertical advection to vertical diffusion (Riley & de Bruyn Kops 2003; Brethouwer *et al.* 2007), in the scaling regime of Riley *et al.* (1981) and Billant & Chomaz (2001).

With these definitions, and recalling the Kolmogorov dissipation scale  $\ell_{\eta} = (\nu^3/\epsilon_V)^{1/4}$ , one can show that  $\mathcal{R}_B = (\ell_{Oz}/\ell_{\eta})^{4/3}$ . In other words, when one wants to measure the intensity of stratified turbulence, the Ozmidov scale plays the role of the integral scale and  $\mathcal{R}_B$  that of the Reynolds number. In particular, when  $\mathcal{R}_B$  is of order one, like in most of the runs shown here (see table 1), the Ozmidov scale coincides with the dissipation scale. Also note that, when  $R_{\omega} \approx 1$ , the small-scale turbulence is at least as vigorous as the imposed rotation frequency (see, e.g. Sagaut & Cambon 2008). These non-dimensional numbers are computed in table 1. Some references (e.g. Smyth & Moum 2000a,b) define the buoyancy Reynolds number as  $\epsilon_V/(\nu N^2)$ . The two definitions should coincide when the characteristic scales satisfy the Taylor relationship  $\epsilon_V = U^3/L$ . For the runs under study here, this dimensional estimate of the energy dissipation rate does not hold, and using the small-scale kinetic

energy dissipation rate, the buoyancy Reynolds number computed with this alternative definition differs from the one given in table 1 (for instance it is of the order of  $10^{-2}$  for the strongly stratified runs with  $\mathcal{R}_B = 1.6$ ). This is consistent with the idea that, for strong stratification, the effective dissipation is related to the dimensional estimate by a  $Fr$  factor.

One of the goals of this paper is to study how the respective role of waves and vortices (see below) depends on the ratio  $N/f$ . Note that there is a range that can be expected to have a special behaviour: when  $1/2 \leq N/f \leq 2$ , there are no three-wave resonances (the simple proof relies on the fact that the inertia–gravity wave frequency  $\sigma(\mathbf{k})$ , defined by (3.4), is bounded by  $f$  and  $N$ ; see for instance Smith & Waleffe (2002), § 6.1). Hence the no-resonance zone separates two regimes:  $N/f < 1/2$  and  $N/f > 2$ . Here we shall focus on the latter range. Note that these two regimes also correspond to cases where the deformation length is respectively smaller and larger than the forcing scale.

### 2.3. Potential vorticity

We define potential vorticity as usual:

$$\Pi = f\partial_z\theta - N\omega_z + \boldsymbol{\omega} \cdot \nabla\theta, \quad (2.6)$$

where  $\boldsymbol{\omega} = \nabla \times \mathbf{u}$  is the standard vorticity. Potential vorticity is a Lagrangian invariant of ideal Boussinesq flows: in the absence of forcing and dissipation, it is conserved along the trajectory of a fluid parcel, as expressed by the equation  $\partial_t\Pi + \mathbf{u} \cdot \nabla\Pi = 0$ . Hence, it is analogous to vertical vorticity in two-dimensional (2D) turbulence, a fundamental difference being that potential vorticity is not a linear functional of the dynamical fields, because of the quadratic term  $\Pi_2 = \boldsymbol{\omega} \cdot \nabla\theta$ , in addition to the linear term  $\Pi_1 = f\partial_z\theta - N\omega_z$ . It follows that, unlike the 2D case, the  $L_2$  norm of potential vorticity, referred to as potential enstrophy and denoted by  $\Gamma$ , is quartic and is not necessarily conserved by the Fourier truncation (see, e.g. Aluie & Kurien 2011). We show in figure 1 the time evolution of potential enstrophy in the two series of runs presented here. In the series of runs at constant Froude number, potential enstrophy decays to approximately 25% of its initial value, then seems to remain constant in time. The decay is faster for higher  $N/f$  ratios, but the final potential enstrophy level is approximately the same for all the runs. In contrast, the series of runs at constant Rossby number exhibits very different levels of potential enstrophy, across approximately three orders of magnitude, and it increases with increasing  $N/f$ , i.e. decreasing Froude number. We conclude from these two graphs that, in the inverse cascade regime studied here, the value of potential enstrophy at late times is a function of the Froude number only. Also, potential enstrophy conservation is better satisfied when stratification is strong. We now introduce the quadratic, cubic and quartic components of potential enstrophy, defined respectively as

$$\Gamma_2 = \int \Pi_1^2, \quad (2.7)$$

$$\Gamma_3 = 2 \int \Pi_1\Pi_2, \quad (2.8)$$

$$\Gamma_4 = \int \Pi_2^2, \quad (2.9)$$



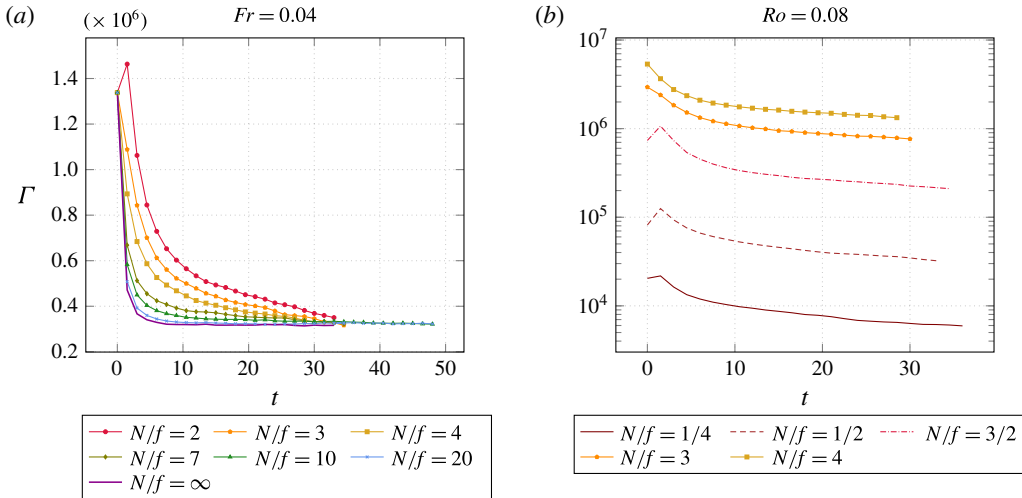


FIGURE 1. (Colour online) Time evolution of the potential enstrophy for the series of runs at constant Froude number (a) and at constant Rossby number (b) with various  $N/f$ . The vertical scale is in logarithmic coordinates for the constant Rossby number series.

such that  $\Gamma = \Gamma_2 + \Gamma_3 + \Gamma_4$ .  $\Gamma_2$ ,  $\Gamma_3$  and  $\Gamma_4$  are respectively quadratic, cubic and quartic in the field variables, but they all have the same physical dimension, that of frequency square or square vorticity. The ratio  $\Gamma_2/\Gamma$  is shown in figure 2. Note that this ratio can exceed unity, since the cubic component of total potential enstrophy is not positive definite (it measures correlations between the linear part of potential vorticity and the nonlinear part). This figure shows that, in all the runs, total potential enstrophy is well approximated by its quadratic part, in agreement with the findings of Kurien & Smith (2014), although it is less and less the case as rotation decreases (constant Froude series of runs) or in the  $N/f = 1/4$  (weak stratification) case, which also has the highest buoyancy Reynolds number of approximately 100 and the smaller deformation length (see table 1). Waite (2013) has argued that in the large- $N/f$  case, total potential enstrophy is dominated by its quadratic part due to viscous effects in the small buoyancy Reynolds number regime. We further discuss the role of viscosity and buoyancy Reynolds number in § 5.

In 2D turbulence, enstrophy conservation has very important consequences: it is ultimately responsible for the inverse cascade. It is a legitimate question to ask whether potential enstrophy conservation places such a strong constraint on rotating-stratified flows. Another important aim of this paper is to show that this constraint is strongly dependent on whether there is rotation or not.

#### 2.4. Inviscid invariants and the direction of the energy cascade

A framework which is quite robust for understanding direct and inverse cascades, introduced by Lee (1952) and Kraichnan (1967), is that of the inviscid invariants of the system. More precisely, the existence of a second definite positive invariant, often quadratic, in addition to energy, may prevent the downscale cascade of energy and lead to an inverse cascade. This is what happens in 2D turbulence (Kraichnan & Montgomery 1980). In stratified turbulence, with or without rotation, there is such a second inviscid invariant, though not quadratic in principle: potential enstrophy  $\Gamma$

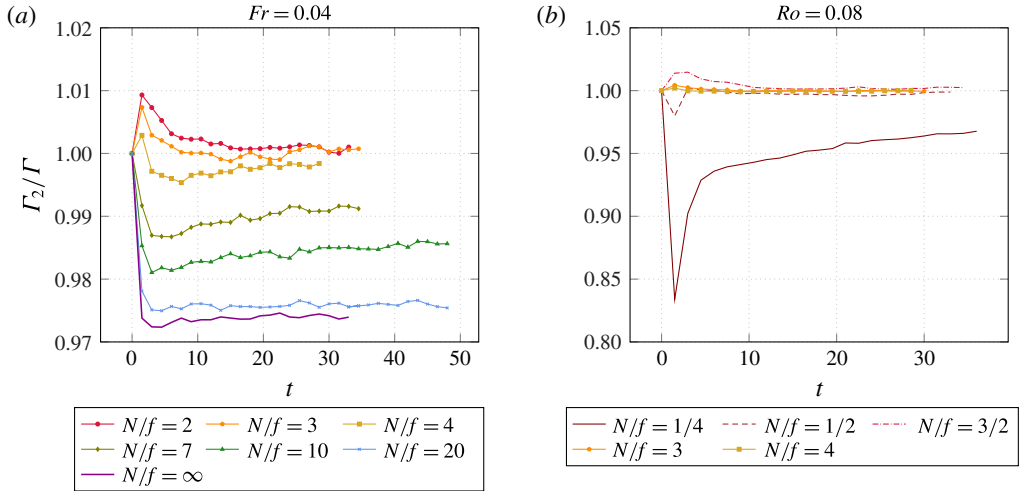


FIGURE 2. (Colour online) Time evolution of the ratio of quadratic potential enstrophy to total potential enstrophy, for the series of runs at constant Froude number (a) and at constant Rossby number (b) with various  $N/f$ .

(see § 2.3). Although this invariant exists regardless of whether there is rotation or not, the phenomenology is not the same: numerical evidence has accumulated over the years (Métais, Riley & Lesieur 1994; Bartello 1995; Métais *et al.* 1996; Lilly *et al.* 1998; Smith & Waleffe 2002; Lindborg 2005; Waite & Bartello 2006*b*; Aluie & Kurien 2011; Marino *et al.* 2013) to show that an inverse cascade in stably stratified flows is only possible when there is sufficient rotation, even though the parameter controlling the transition remains unclear. A subtlety here is that the second invariant has constant sign (it is always positive), but is not definite: some combinations of the fields make potential vorticity vanish. Such combinations correspond to the wave modes (see § 3). Hence, a natural way of thinking is to say that if waves and slow modes did not exchange energy, the wave and slow mode energy would be separately conserved, and slow modes would have invariants similar to 2D turbulence, while waves would have invariants similar to 3D homogeneous isotropic turbulence. Therefore, in that case one should expect an inverse cascade of slow mode energy and a direct cascade of wave energy. This idea was formulated in pioneering studies such as those of Warn (1986), Bartello (1995) and Waite & Bartello (2004).

However, in the purely stratified case, this reasoning does not hold since then, potential enstrophy is still degenerate even when we restrict it to the slow modes. Indeed, in the non-rotating case, only slow modes with  $k_{\perp} \neq 0$  contribute to potential enstrophy (see § 3.3). This peculiarity was used in a statistical mechanics argument (Herbert *et al.* 2014) in order to explain why the two cases have opposite cascade directions in spite of having the same inviscid invariants. From this point of view, it could also be because of the presence of the vertically sheared horizontal flow modes that stratified turbulence does not have an inverse cascade.

A major goal of this work is to study how the roles played by slow modes and waves in the inverse cascade, inferred from the above reasoning on the inviscid invariants, evolve when non-dimensional parameters vary, and how the mechanisms described in this section come into play to break the inverse cascade when stratification dominates.

### 3. Waves and vortices: normal mode decomposition

#### 3.1. The linear dynamics

Inertia–gravity wave dynamics has been studied for a long time (see for example Hasselmann 1966; Garrett & Munk 1979; Müller *et al.* 1986; Bartello 1995; Staquet & Sommeria 2002) and is summarized very briefly here in order to recall essential concepts and to define notations. Indeed, the linear terms introduced by the Coriolis force and the buoyancy force in (2.1)–(2.3) allow for the propagation of dispersive waves. The linearized inviscid and unforced dynamics reads:

$$\partial_t \mathbf{u} = -\nabla P - f \mathbf{e}_z \times \mathbf{u} - N\theta \mathbf{e}_z, \tag{3.1}$$

$$\partial_t \theta = Nu_z, \tag{3.2}$$

$$\nabla \cdot \mathbf{u} = 0. \tag{3.3}$$

This set of equations corresponds to the low-Froude-number limit ( $Fr \rightarrow 0$ ) of the Boussinesq equations, if we assume that the time scale is the buoyancy time scale  $N^{-1}$  (Lilly 1983). The above equations admit travelling wave solutions of the form  $u_j(\mathbf{x}, t) = U_j e^{i(\mathbf{k} \cdot \mathbf{x} - \sigma(k)t)}$ ,  $\theta(\mathbf{x}, t) = \Theta e^{i(\mathbf{k} \cdot \mathbf{x} - \sigma(k)t)}$ ,  $P = P_0 e^{i(\mathbf{k} \cdot \mathbf{x} - \sigma(k)t)}$ , for arbitrary wave vector  $\mathbf{k}$ , with relations between the complex amplitudes  $U_j$ ,  $\Theta$ ,  $P_0$  fixed by the above equations, and with the dispersion relation

$$\sigma(\mathbf{k}) = \sqrt{f^2 k_{\parallel}^2 / k^2 + N^2 k_{\perp}^2 / k^2}. \tag{3.4}$$

Such waves are called inertia–gravity waves (and include, of course, waves travelling in the  $-\mathbf{k}$  direction). Note that although the Coriolis parameter only appears in the evolution equation for the horizontal velocity, and the Brunt–Väisälä frequency only for the vertical velocity and temperature, inertia–gravity waves couple the four dynamical fields because of the incompressibility condition. Without pressure, we would simply have inertial oscillations, at frequency  $f$ , for the horizontal velocity, decoupled from gravity waves of frequency  $N$  acting on the vertical velocity and the temperature.

The nonlinear term introduces a coupling between waves with different wave vectors. A possible approach is to treat the dynamical fields as a wave field with slow nonlinear evolution of the magnitude of each wave mode, using a perturbative approach. Resonant interactions (Longuet-Higgins, Gill & Kenyon 1967; Newell 1969) offer a natural way to close the hierarchy of moments. This is a first kind of turbulence, referred to as wave turbulence (Zakharov, Lvov & Falkovich 1992; Nazarenko 2010; Newell & Rumpf 2011).

Now, the set of linearized equations also admits stationary solutions, where the right-hand side of (3.1)–(3.2) vanishes. These solutions have no vertical velocity ( $u_z = 0$ ), and the pressure gradient balances at the same time the Coriolis force (geostrophic balance,  $\nabla_{\perp} P = -f \mathbf{e}_z \times \mathbf{u}$ ) and the buoyancy force (hydrostatic balance,  $\partial_z P = -N\theta \mathbf{e}_z$ ). In other words, rotation and stratification act to maintain horizontal motion. This kind of balanced motion can also be seen as a low-Froude-number limit ( $Fr \rightarrow 0$ ) solution of the Boussinesq equations, assuming that  $Bu = 1$  and that the time scale is the eddy turnover time (Lilly 1983). It corresponds to eddies of typical aspect ratio  $f/N$ , which are advected by the horizontal velocity field, much like vortices in 2D turbulence. Hence, another kind of turbulence, referred to as geostrophic turbulence, is encapsulated in the Boussinesq equations.

3.2. The normal mode decomposition in Fourier space

The two kinds of motion, waves and vortices, described above, correspond to normal modes of the linearized Boussinesq equations. Although they are coupled in the nonlinear dynamics, they provide a useful framework for analysing the full system. Here, we shall try to disentangle the behaviour of these two contributions in the simulated fields. To separate the two contributions, it is convenient to express them in Fourier space (Bartello 1995, see also Herbert *et al.* 2014): we introduce  $\mathcal{B} = \mathbb{Z}^3$  the set of wave vectors, and for each wave vector  $\mathbf{k} \in \mathcal{B}$ , the vectors

$$\mathbf{Z}_0(\mathbf{k}) = \mathbf{M}(\mathbf{k}) \begin{pmatrix} 0 \\ 1 \\ 0 \end{pmatrix}, \quad \mathbf{Z}_-(\mathbf{k}) = \mathbf{M}(\mathbf{k}) \begin{pmatrix} 1 \\ 0 \\ 0 \end{pmatrix}, \quad \text{and} \quad \mathbf{Z}_+(\mathbf{k}) = \mathbf{M}(\mathbf{k}) \begin{pmatrix} 0 \\ 0 \\ 1 \end{pmatrix}, \quad (3.5a-c)$$

where the expression of the matrix  $\mathbf{M}(\mathbf{k})$  is given by:

$$\mathbf{M}(\mathbf{k}) = \begin{cases} \frac{1}{\sqrt{2}kk_\perp\sigma(\mathbf{k})} \begin{pmatrix} fk_2k_\parallel - ik_1k_\parallel\sigma(\mathbf{k}) & -\sqrt{2}Nk_2k_\perp & fk_2k_\parallel + ik_1k_\parallel\sigma(\mathbf{k}) \\ -fk_1k_\parallel - ik_2k_\parallel\sigma(\mathbf{k}) & \sqrt{2}Nk_1k_\perp & -fk_1k_\parallel + ik_2k_\parallel\sigma(\mathbf{k}) \\ ik_\perp^2\sigma(\mathbf{k}) & 0 & -ik_\perp^2\sigma(\mathbf{k}) \\ -Nk_\perp^2 & -\sqrt{2}fk_\parallel k_\perp & -Nk_\perp^2 \end{pmatrix} & \text{if } k_\perp \neq 0, \\ \frac{1}{\sqrt{2}} \begin{pmatrix} i & 0 & -i \\ 1 & 0 & 1 \\ 0 & 0 & 0 \\ 0 & -\sqrt{2} & 0 \end{pmatrix} & \text{if } k_\perp = 0. \end{cases} \quad (3.6)$$

The vectors  $\mathbf{Z}_0(\mathbf{k}), \mathbf{Z}_-(\mathbf{k})$  and  $\mathbf{Z}_+(\mathbf{k})$  are mutually orthogonal, and normalized to unity:

$$\mathbf{Z}_r(\mathbf{k})^\dagger \mathbf{Z}_s(\mathbf{k}) = \delta_{rs}, \quad (3.7)$$

where  $\dagger$  denotes the transpose and complex conjugation. Although the matrix  $\mathbf{M}(\mathbf{k})$  is rectangular, it satisfies the hermitian identity  $\mathbf{M}(\mathbf{k})^\dagger \mathbf{M}(\mathbf{k}) = I_3$ . They are the normal modes of the linearized dynamics: their evolution in the linearized dynamics is given by

$$\mathbf{L}(\mathbf{k})\mathbf{Z}_0(\mathbf{k}) = 0, \quad (3.8)$$

$$\mathbf{L}(\mathbf{k})\mathbf{Z}_+(\mathbf{k}) = i\sigma(\mathbf{k})\mathbf{Z}_+(\mathbf{k}), \quad (3.9)$$

$$\mathbf{L}(\mathbf{k})\mathbf{Z}_-(\mathbf{k}) = -i\sigma(\mathbf{k})\mathbf{Z}_-(\mathbf{k}), \quad (3.10)$$

where  $\mathbf{L}(\mathbf{k})$  is the linear operator in Fourier space associated to the linearized dynamics give by (3.1)–(3.3). We see that the mode  $\mathbf{Z}_0(\mathbf{k})$  is conserved by the linear dynamics, while the modes  $\mathbf{Z}_\pm(\mathbf{k})$ , corresponding to the inertia–gravity waves, propagate with frequency  $\sigma(\mathbf{k})$ . Therefore,  $\mathbf{Z}_0$ , whose characteristic evolution time is the eddy turnover time, is referred to as the slow mode. The normal modes can be used as a basis for the Fourier modes of the dynamical fields. Introducing the Fourier decomposition of the velocity and temperature fields

$$u_i(\mathbf{x}) = \sum_{\mathbf{k} \in \mathcal{B}} \hat{u}_i(\mathbf{k}) e^{i\mathbf{k} \cdot \mathbf{x}}, \quad (3.11)$$

$$\theta(\mathbf{x}) = \sum_{\mathbf{k} \in \mathcal{B}} \hat{\theta}(\mathbf{k}) e^{i\mathbf{k} \cdot \mathbf{x}}, \quad (3.12)$$

and denoting  $X(\mathbf{k}) = (\hat{u}_1(\mathbf{k}), \hat{u}_2(\mathbf{k}), \hat{u}_3(\mathbf{k}), \hat{\theta}(\mathbf{k}))$  the Fourier coefficients for wave vector  $\mathbf{k}$ , they can be expressed as a linear combination of the normal modes:

$$X(\mathbf{k}) = A_0(\mathbf{k})Z_0(\mathbf{k}) + A_-(\mathbf{k})Z_-(\mathbf{k}) + A_+(\mathbf{k})Z_+(\mathbf{k}), \tag{3.13}$$

$$= \mathbf{M}(\mathbf{k}) \underbrace{\begin{pmatrix} A_-(\mathbf{k}) \\ A_0(\mathbf{k}) \\ A_+(\mathbf{k}) \end{pmatrix}}_{A(\mathbf{k})}. \tag{3.14}$$

Introducing the projectors  $\mathbf{P}_0(\mathbf{k}) = Z_0(\mathbf{k})Z_0(\mathbf{k})^\dagger$  and  $\mathbf{P}_W(\mathbf{k}) = Z_-(\mathbf{k})Z_-(\mathbf{k})^\dagger + Z_+(\mathbf{k})Z_+(\mathbf{k})^\dagger$ , we have of course  $\mathbf{P}_0(\mathbf{k})X(\mathbf{k}) = A_0(\mathbf{k})Z_0(\mathbf{k})$  and  $\mathbf{P}_W(\mathbf{k})X(\mathbf{k}) = A_-(\mathbf{k})Z_-(\mathbf{k}) + A_+(\mathbf{k})Z_+(\mathbf{k})$ , and the two projectors are mutually orthogonal, so that  $\mathbf{P}_0(\mathbf{k}) \oplus \mathbf{P}_W(\mathbf{k}) = I_4$ . Denoting  $\mathcal{F} : (u_1, u_2, u_3, \theta) \mapsto (\hat{u}_1, \hat{u}_2, \hat{u}_3, \hat{\theta})$ , with  $\hat{x} : \mathbf{k} \in \mathcal{B} \mapsto \hat{x}(\mathbf{k}) \in \mathbb{C}$ , the Fourier transform, and  $\hat{\mathcal{P}}_0 : (\hat{u}_1, \hat{u}_2, \hat{u}_3, \hat{\theta}) \mapsto (\mathbf{k} \mapsto \mathbf{P}_0(\mathbf{k})X(\mathbf{k}))$ ,  $\hat{\mathcal{P}}_W : (\hat{u}_1, \hat{u}_2, \hat{u}_3, \hat{\theta}) \mapsto (\mathbf{k} \mapsto \mathbf{P}_W(\mathbf{k})X(\mathbf{k}))$ , the operators  $\mathcal{P}_0 = \mathcal{F}^{-1} \circ \hat{\mathcal{P}}_0 \circ \mathcal{F}$  and  $\mathcal{P}_W = \mathcal{F}^{-1} \circ \hat{\mathcal{P}}_W \circ \mathcal{F}$  are mutually orthogonal projectors acting on the set of dynamical fields:

$$\mathcal{P}_0^2 = \mathcal{P}_0, \quad \mathcal{P}_W^2 = \mathcal{P}_W, \tag{3.15a,b}$$

$$\mathcal{P}_0\mathcal{P}_W = \mathcal{P}_W\mathcal{P}_0 = 0, \quad \mathcal{P}_0 \oplus \mathcal{P}_W = \text{Id}. \tag{3.16a,b}$$

Hence, we may write  $\mathbf{u} = \mathbf{u}_0 + \mathbf{u}_W$  and  $\theta = \theta_0 + \theta_W$ , with  $(u_0^1, u_0^2, u_0^3, \theta_0) = \mathcal{P}_0(u^1, u^2, u^3, \theta)$ , and  $(u_W^1, u_W^2, u_W^3, \theta_W) = \mathcal{P}_W(u^1, u^2, u^3, \theta)$ . It is easily checked that the projection on the slow modes defined above has vanishing vertical velocity:  $u_0^3 = 0$ , and is divergence free:  $\nabla \cdot \mathbf{u}_0 = \nabla_\perp \cdot \mathbf{u}_0 = 0$ . The explicit expression in real space of the projection operators introduced above is given by Whitehead & Wingate (2014). They also describe the projection operators on the slow manifolds obtained in the limit of rapid rotation and weak stratification on the one hand, and strong stratification and weak rotation on the other hand.

It follows from the above that the total energy

$$E_T = \frac{1}{2} \int (\mathbf{u}^2 + \theta^2) = \frac{1}{2} \sum_{\mathbf{k} \in \mathcal{B}} X(\mathbf{k})^\dagger X(\mathbf{k}) = \frac{1}{2} \sum_{\mathbf{k} \in \mathcal{B}} A(\mathbf{k})^\dagger A(\mathbf{k}) \tag{3.17}$$

breaks up in two pieces:  $E_T = E_0 + E_W$ , where  $E_0$  is the energy in the slow modes:

$$E_0 = \frac{1}{2} \int (\mathbf{u}_0^2 + \theta_0^2) = \frac{1}{2} \sum_{\mathbf{k} \in \mathcal{B}} |A_0(\mathbf{k})|^2 = \frac{1}{2} \sum_{\mathbf{k} \in \mathcal{B}} E_0(\mathbf{k}), \tag{3.18}$$

and  $E_W$  the energy in the wave modes:

$$E_W = \frac{1}{2} \int (\mathbf{u}_W^2 + \theta_W^2) = \frac{1}{2} \sum_{\mathbf{k} \in \mathcal{B}} [|A_-(\mathbf{k})|^2 + |A_+(\mathbf{k})|^2] = \frac{1}{2} \sum_{\mathbf{k} \in \mathcal{B}} E_W(\mathbf{k}). \tag{3.19}$$

Note that, due to the orthogonality property of the projections, the cross-terms in physical space cancel out:  $\int \mathbf{u}_0 \cdot \mathbf{u}_W + \int \theta_0\theta_W = 0$ . However, these terms do not vanish individually. In other words, the vector  $(\mathbf{u}_0, \theta_0)$  is indeed orthogonal to the vector  $(\mathbf{u}_W, \theta_W)$ , but this does not imply that the vector  $\mathbf{u}_0$  is orthogonal to  $\mathbf{u}_W$ , where orthogonality refers to the canonical scalar product in each of these two Hilbert spaces. A consequence is that care should be taken when trying to mix decomposition of the energy in terms of kinetic/potential energy and in terms of vortical/wave modes. Here, we shall avoid altogether distinguishing between kinetic and potential energy.

### 3.3. Normal mode decomposition, balance and potential vorticity

As can be checked explicitly (Herbert *et al.* 2014, e.g.), in the linear framework, the slow modes satisfy balance relations: in the presence of rotation, they are in both geostrophic and hydrostatic balance. By contrast, for purely stratified flows, the slow modes are not in hydrostatic balance, except for purely vertical wave vectors, i.e. for horizontally homogeneous modes (the VSHF modes, see § 4.3). Of course, nonlinear effects break these relations, and a flow initialized in the image of the projector  $\mathcal{P}_0$  (i.e. containing no wave modes initially) will eventually lose balance and radiate inertia–gravity waves. If one is interested in maintaining the balance relations, as much as possible, without generating such oscillations, the initial state should contain a wave component designed to compensate the nonlinear effects; such nonlinear initialization procedures have been designed in numerical weather prediction (Baer & Tribbia 1977; Leith 1980). Alternatively, balanced models, where the dynamics of the waves is slaved to that of the slow modes, can be written to remain on a slow manifold in phase space (Warn *et al.* 1995; Vanneste 2013). For the sake of simplicity, we shall be content here with projecting the data on the vector space spanned by the slow modes (which can be seen geometrically as a tangent subspace for the slow manifold, or as a zeroth-order approximation to the slow manifold) and its orthogonal subspace, spanned by the wave modes, as defined above. This means that although the normal modes introduced above are always well defined, care should be taken when interpreting the projections in terms of balance relations.

The normal modes are also related to potential vorticity. An argument due in particular to Smith & Waleffe (2002) relies on the fact that in the linear dynamics,  $\Pi_1$  is a point-wise invariant:  $\partial_t \Pi_1 = 0$ . It follows, by applying the Fourier transform in both space and time, that  $\sigma \hat{\Pi}_1(\mathbf{k}, \sigma) = 0$ , where  $\sigma$  is the time frequency. Hence, wave modes, for which  $\sigma(\mathbf{k}) \neq 0$  must have  $\hat{\Pi}_1(\mathbf{k}, \sigma) = 0$ , while vortical modes (i.e. by definition, those for which  $\hat{\Pi}_1(\mathbf{k}, \sigma) \neq 0$ ) must have zero frequency. In fact, it is easily shown that, in general, the identity  $\hat{\Pi}_1(\mathbf{k}, t) = -ik\sigma(\mathbf{k})A_0(\mathbf{k}, t)$  holds, and therefore (Bartello 1995; Herbert *et al.* 2014):

$$\Gamma_2 = \sum_{\mathbf{k} \in \mathcal{B}} k^2 \sigma(\mathbf{k})^2 |A_0(\mathbf{k})|^2. \quad (3.20)$$

It follows that, even when considering the full nonlinear dynamics, waves do not carry any linear potential vorticity. Similarly, we know that in the presence of rotation, all the slow modes contribute to linear potential vorticity. In the purely stratified case, however, the slow component of the VSHF modes ( $k_\perp = 0$ ) contributes neither to linear potential vorticity, nor, therefore, to quadratic potential enstrophy  $\Gamma_2$ . All the other slow modes still carry linear potential vorticity.

The fact that the connection between slow modes and vortical modes (i.e. modes which contribute to linear potential vorticity) does not depend on whether we are considering the linear or the full nonlinear dynamics, while the connection between slow modes and balanced modes does, is due to the kinematic nature of the connection between linear potential vorticity and the dynamical fields. By contrast, the notion of balance is dynamical in the sense that it involves pressure, which is determined by the equations of motion. When including the nonlinear term in the dynamics, another component of pressure appears, which breaks the balance relations.

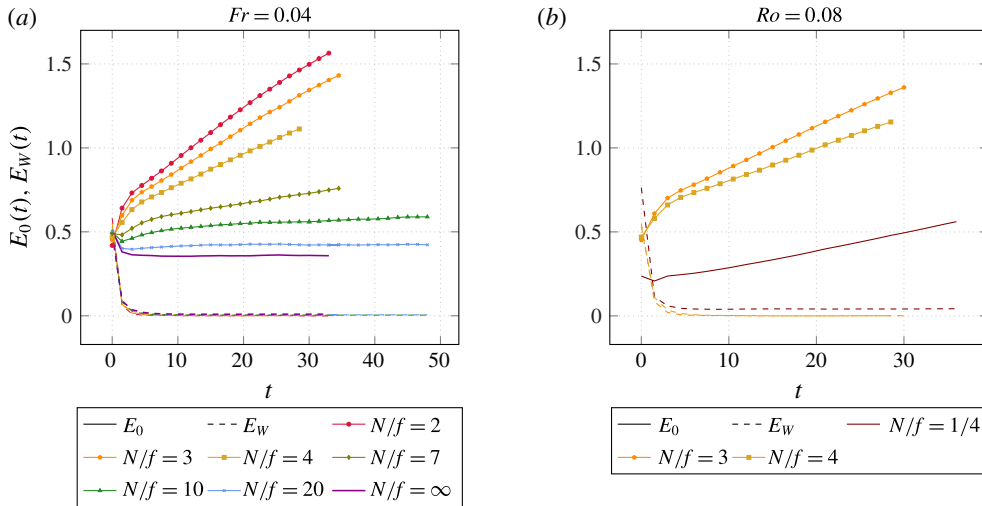


FIGURE 3. (Colour online) Time evolution of the wave (dashed lines) and vortical (solid lines) parts of the total energy for the series of runs at constant Froude number (a) and at constant Rossby number (b) with various  $N/f$ . Runs within the no-resonance zone have been excluded for clarity. Note that the curves corresponding to the decay of the wave energy almost collapse onto a single curve: see figure 5 for a figure in logarithmic coordinates where they can be distinguished.

#### 4. Partition of energy between slow and wave modes

##### 4.1. Time evolution of global quantities

The time evolution of the two energy components, wave and vortical, is shown in figure 3 (see also figure 5) for the series of runs at constant Froude number (a) and at constant Rossby number (b), excluding the runs for which the three-wave resonances are suppressed. Although the initial conditions all have approximately the same energy in each component, we see that, in all the runs, the wave energy decays very fast and the slow modes dominate, even for the runs that do not undergo a strong inverse cascade (in the purely stratified case, there is no inverse cascade at all). This is also true for the runs in the series at constant Rossby number (figure 3b) and in the no-resonance zone (not shown). After an initial phase, we observe in the runs for which  $N/f$  is small enough ( $N/f \leq 10$ ) a linear growth of the energy in the slow modes, characteristic of an inverse cascade. For  $N/f \geq 2$ , the growth rate appears to be a decreasing function of  $N/f$ , and this is confirmed by plotting the time average of the time derivative of the energy in the slow modes (figure 4a). This figure also confirms that the growth rate vanishes at  $N/f = 20$  or in the purely stratified case (see also Marino *et al.* (2014)). There is also a linear growth of the energy in the slow modes for the runs in the no-resonance zone in the series at constant Froude and for all the runs in the series at constant Rossby. For both series of runs, the growth rate appears to reach a maximum located inside the no-resonance zone (figure 4a). In addition, the growth rate seems to depend primarily on  $N/f$  rather than the Froude and Rossby numbers. These conclusions are consistent with the analysis of the time evolution of the kinetic energy obtained earlier (Marino *et al.* 2013). Figure 4(b) summarizes how the fraction of energy in the slow modes, averaged in time (over all the snapshots following the peak of enstrophy), evolves as a function of  $N/f$ . Surprisingly, the case

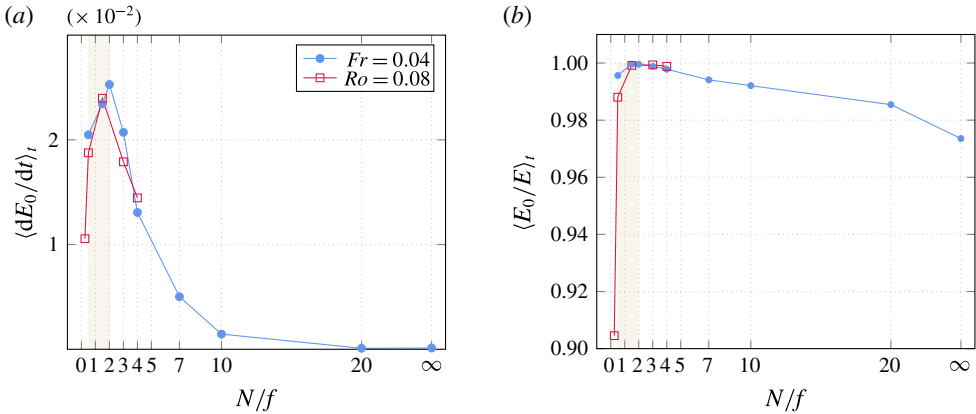


FIGURE 4. (Colour online) (a) Time-averaged growth rate of the energy in the slow modes as a function of  $N/f$ , for the two series of runs, at constant Froude number (circles) and at constant Rossby number (squares), respectively. (b) Time-averaged fraction of energy in the slow modes as a function of  $N/f$ , for the two series of runs, at constant Froude number (circles) and at constant Rossby number (squares), respectively. The no-resonance zone is the shaded area.

where this fraction attains its minimum value, although it is still approximately 0.9, is not the purely stratified case, but the rotation-dominated case  $N/f = 1/4$ , which also has the highest  $\mathcal{R}_B$  and the smallest deformation length. One should keep in mind, however, that the ratio will keep increasing towards unit value for all the runs which exhibit a growth of  $E_0$ . Many of the runs are already very close to this limit value, and for the runs which do not exhibit such a growth of  $E_0$ , the ratio would not change with longer integration times. Since figure 3 does not allow one to distinguish the different curves for the wave energy at various  $N/f$  ratios, we show this quantity in logarithmic scale in figure 5. For values of  $N/f$  above 7 (this is also true for the case  $N/f = 1/4$ ), we see a decay phase followed by a regime where the level of energy in the waves stays constant. For the other  $N/f$  values, the wave energy drops suddenly at the end of the decay phase, then increases back to more or less its value before the drop, and seems to stay constant afterwards. Although the time resolution is not sufficient for precise measurements, the decay seems to follow roughly a power law, and it is steeper for smaller  $N/f$  ratios (except for the  $N/f = 1/4$  and  $N/f = 1/2$  cases, at substantially higher  $\mathcal{R}_B$ ).

#### 4.2. Spectral analysis

We show in figure 6 the isotropic spectra of energy in the wave and slow modes, denoted respectively  $E_W(k)$  and  $E_0(k)$ , for the series of runs at constant Froude number. The isotropic spectra are defined, as usual, as integrals over spherical shells in Fourier space:

$$E_0(k) = \int_{\|\mathbf{k}\|=k} |A_0(\mathbf{k})|^2 d\mathbf{k}, \quad E_W(k) = \int_{\|\mathbf{k}\|=k} [|A_+(\mathbf{k})|^2 + |A_-(\mathbf{k})|^2] d\mathbf{k}. \quad (4.1a,b)$$

For all the runs, at early times ( $t = 1.5$ , before the peak of enstrophy), the slow mode component dominates at large scales while the wave component dominates at small



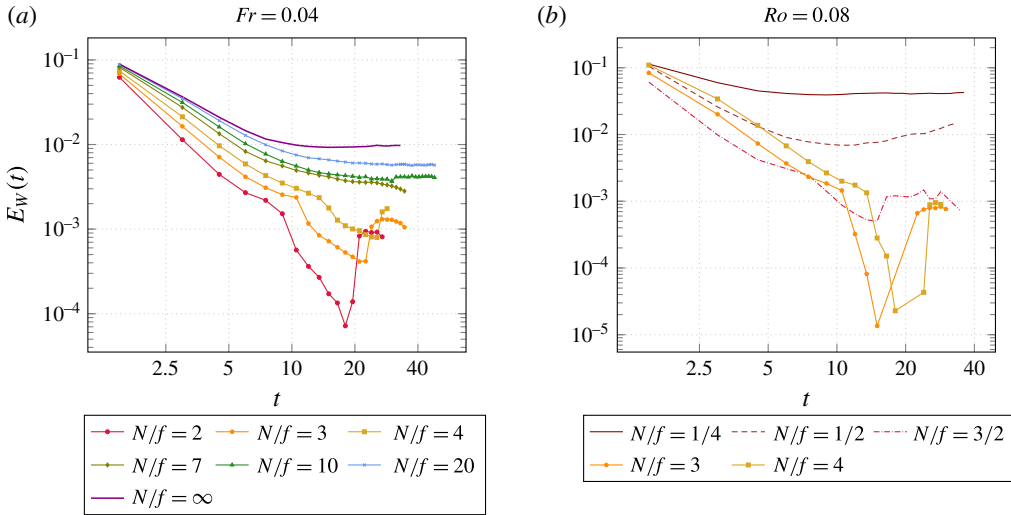


FIGURE 5. (Colour online) Time evolution of the wave component of the total energy in logarithmic coordinates, for the series of runs at constant Froude number (a) and at constant Rossby number (b) with various  $N/f$ .

scales. Note that the wavenumber at which the two spectra cross increases with  $N/f$ . When the turbulence develops, the wave energy spectrum decays rapidly, including at small scales, and the slow mode spectrum dominates at all scales. However, the wave energy at small scales increases when  $N/f$  increases. The other salient feature of the isotropic energy spectra is the growth of the slow mode energy at scales larger than the forcing scale. In most of the runs, up to approximately  $N/f = 7$ , this growth takes the form of an inverse cascade, with a spectral slope that is consistent with  $k^{-5/3}$ . However, the inverse cascade of the slow modes weakens as  $N/f$  increases, as already found from the analysis of global quantities. Already, at  $N/f = 7$ , the spectrum at the final time of the simulation has a narrow  $k^{-5/3}$  range, and at  $N/f = 10$ , the energy in the slow modes seems to saturate at large scale with a flat spectrum  $k^0$ . Note that we cannot rule out completely the possibility that the  $-5/3$  range would extend further towards large scales with a larger integration time. However, it should be noted that the growth rate of the energy in the slow modes for these values of  $N/f$  is very small (see figure 4) and that the slow mode energy spectrum has not evolved much between  $t = 22.5$  and  $t = 30$ . This indicates that even if the  $-5/3$  range was to extend towards larger scales, it would require a very long integration time. Besides, the growth does not seem to be self-similar, since the spectral slope at scales larger than the  $-5/3$  range becomes shallower (almost flat), unlike traditional inverse cascade phenomena. The flat spectrum for slow mode energy at large scales is the only notable feature of the  $N/f = 20$  run, and it is also present in the purely stratified run, although in that case there is an accumulation of energy in the  $k = 1$  modes. Such a flat spectrum has already been observed for kinetic energy in Smith & Waleffe (2002) for  $N/f = 10$  (see also Kimura & Herring (2012) and Marino *et al.* (2013, 2014)).

The transition between these two scenarios is further described in figure 10, which shows the spectral slope  $\alpha$  of the isotropic energy spectrum of the slow modes at large scale, defined by  $E_0(k) \sim k^\alpha$  for  $k \leq k_F$ , and computed numerically by a least-squares fit, as a function of  $N/f$ . This figure shows that the transition appears to be continuous,

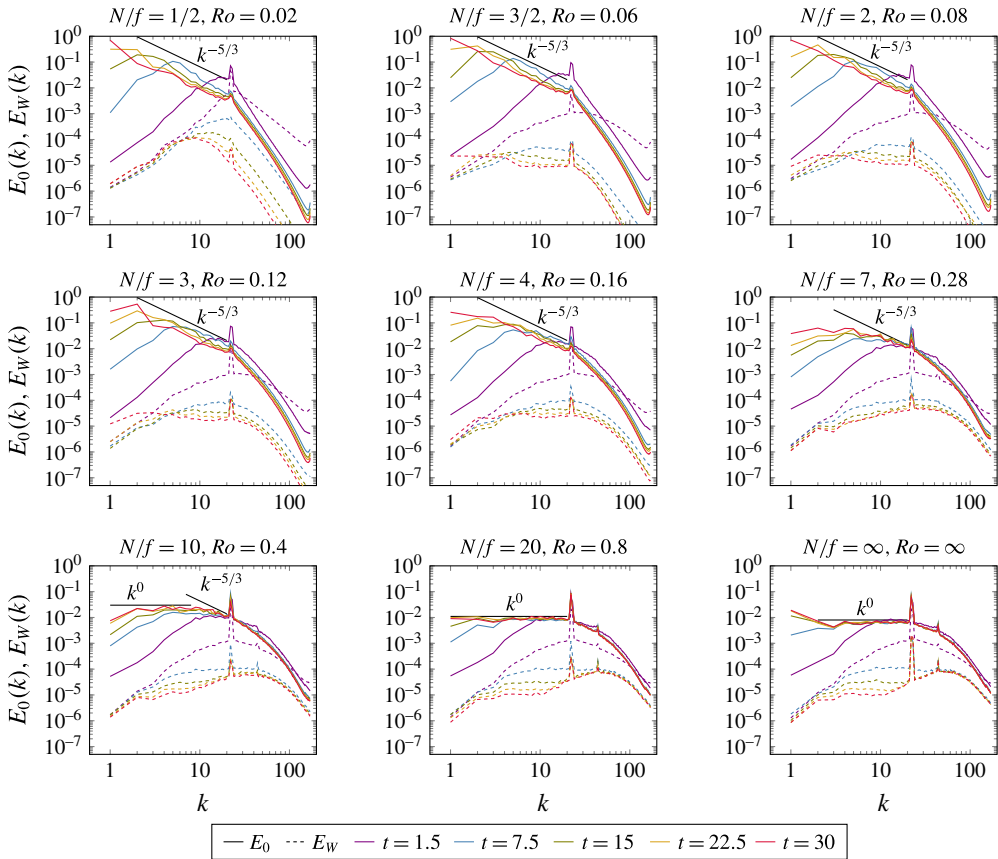


FIGURE 6. (Colour online) Isotropic energy spectra of the wave (solid lines) and slow mode (dashed lines) for the series of runs with constant Froude number ( $Fr = 0.04$ ) and varying  $N/f$ . The times shown are indicated in the legend at the bottom, going from purple to blue, green, yellow and red in increasing order. Two different spectral laws are indicated as well for comparison.

although the specific values of the spectral slopes lack in accuracy since the inertial range is rather short (remember that  $k_F \in [22, 23]$ ), and since they may depend on the details of the least-squares fitting procedure: choice of snapshot, excluding the  $k = 1$  modes to get rid of the formation of a possible condensate at the largest scale, . . . . In particular, no time averaging has been performed here. Higher resolutions would also provide improvements in accuracy. Another caveat is that, as noted above, the intermediate values (e.g.  $N/f = 7$  or 10) may move closer to  $-5/3$  with a larger integration time.

The inverse cascade of the slow mode energy spectrum is also seen in the series of runs at constant Rossby number (figure 7). Interestingly, for the runs with small  $N/f$  ratios ( $N/f = 1/4$  or  $1/2$ ), i.e. the runs with the highest Froude numbers, the waves dominate at small scales even at late times, when these scales seem to have attained stationarity. This is probably a consequence of the higher buoyancy Reynolds number, rather than the Burger number or the deformation length (see the discussion in § 5.2).

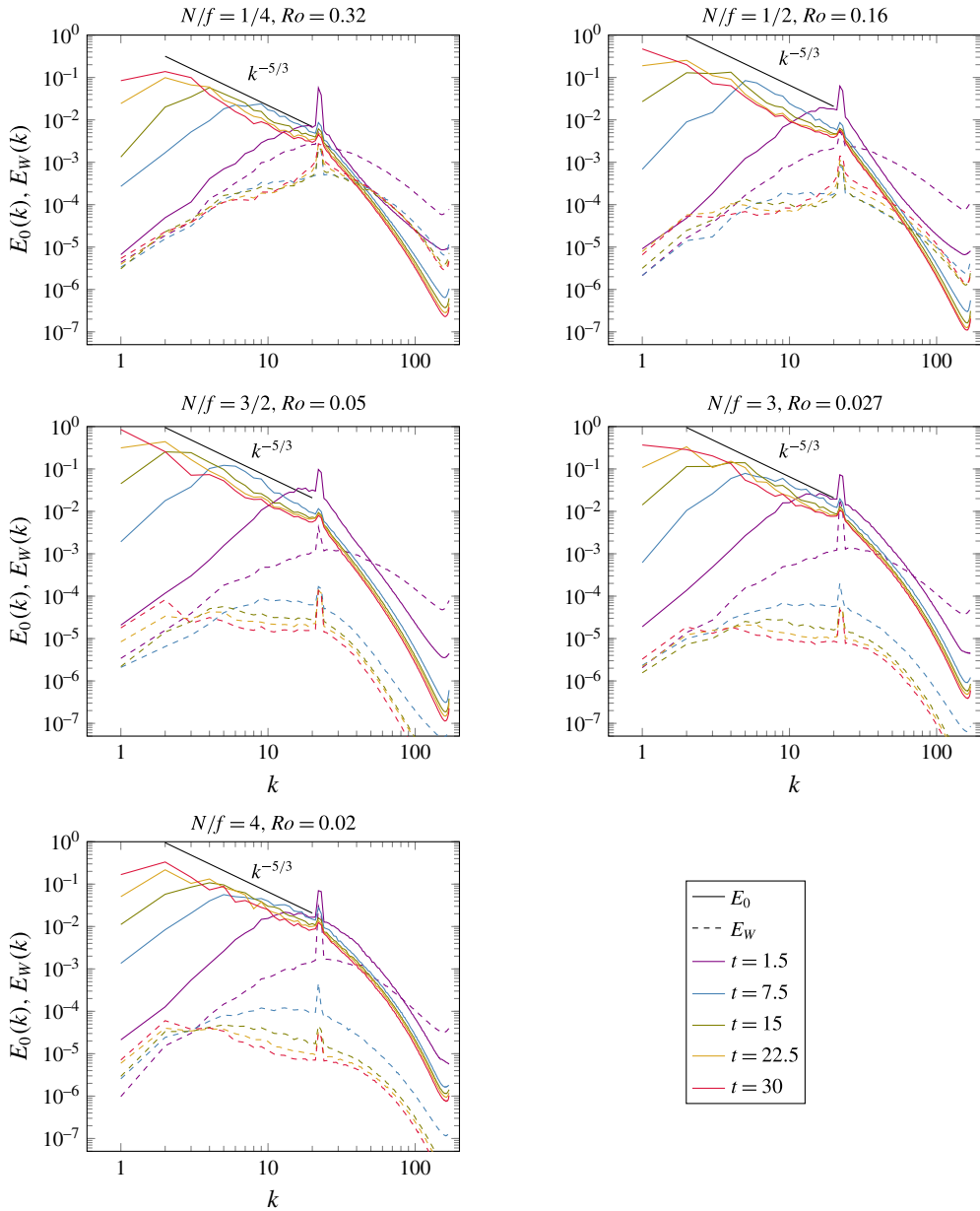


FIGURE 7. (Colour online) Isotropic spectra of the wave and slow mode components of energy for the series of runs with constant Rossby number ( $Ro = 0.08$ ) and varying  $N/f$ . The symbols are the same as in figure 6.

In addition to the isotropic spectrum, obtained by summing over spherical shells in Fourier space, it is always relevant for anisotropic flows to compute the so-called reduced spectra, where the summation is done either on cylinders (fixed  $k_{\perp}$ ) or planes (fixed  $k_{\parallel}$ ) in Fourier space (see e.g. Godefert & Staquet 2003; Sagaut & Cambon 2008; Mininni 2011; Mininni *et al.* 2012; Marino *et al.* 2014). Introducing the axisymmetric spectra  $e_0(k_{\perp}, k_{\parallel})$ ,  $e_W(k_{\perp}, k_{\parallel})$  defined by

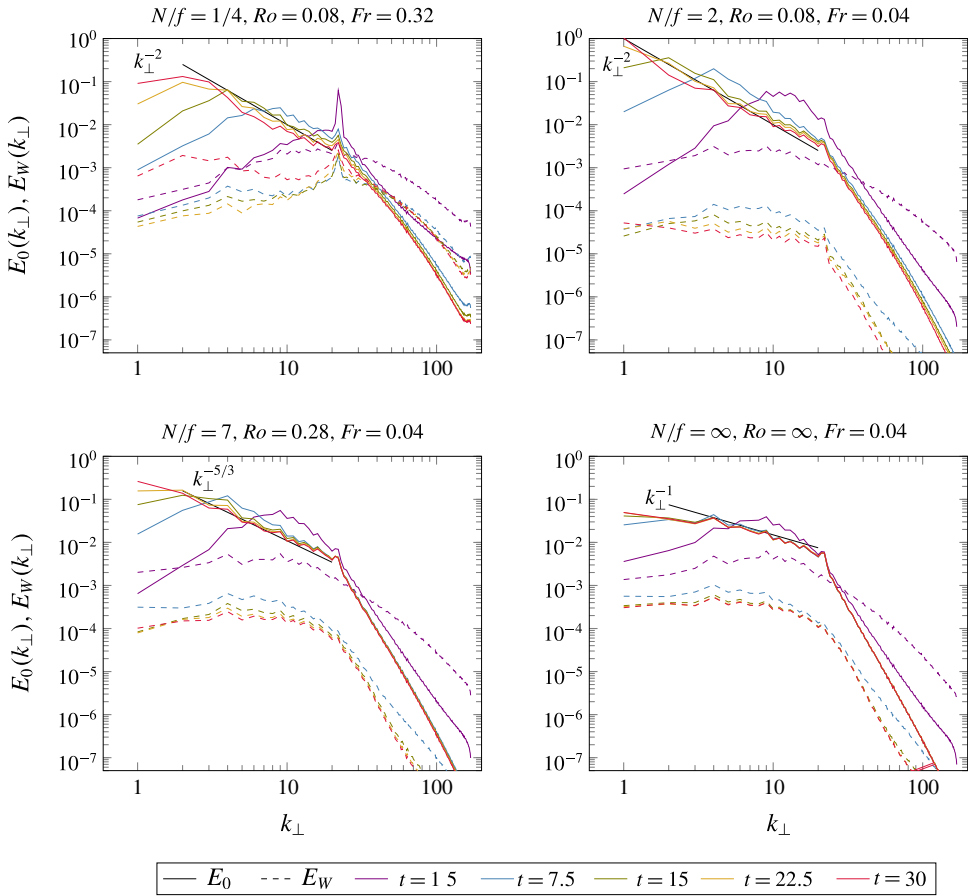


FIGURE 8. (Colour online) Perpendicular spectra of the wave and slow mode components of energy for selected values of the parameters. Scaling laws are represented only for reference. Line encoding and colours are similar to the two preceding figures.

$$e_0(k_{\perp}, k_{\parallel}) = \int_0^{2\pi} |A_0(k_{\perp} \cos \phi \mathbf{e}_x + k_{\perp} \sin \phi \mathbf{e}_y + k_{\parallel} \mathbf{e}_z)|^2 k_{\perp} d\phi, \tag{4.2}$$

$$e_W(k_{\perp}, k_{\parallel}) = \int_0^{2\pi} [|A_+(k_{\perp} \cos \phi \mathbf{e}_x + k_{\perp} \sin \phi \mathbf{e}_y + k_{\parallel} \mathbf{e}_z)|^2 + |A_-(k_{\perp} \cos \phi \mathbf{e}_x + k_{\perp} \sin \phi \mathbf{e}_y + k_{\parallel} \mathbf{e}_z)|^2] k_{\perp} d\phi, \tag{4.3}$$

the perpendicular and parallel spectra are defined as follows for each type of mode,  $s = 0, W$ :

$$E_s(k_{\perp}) = \int_0^{k_{max}} e_s(k_{\perp}, k_{\parallel}) dk_{\parallel}, \quad E_s(k_{\parallel}) = \int_0^{k_{max}} e_s(k_{\perp}, k_{\parallel}) dk_{\perp}. \tag{4.4a,b}$$

Figure 8 shows the perpendicular spectrum of energy in the wave ( $E_W(k_{\perp})$ ) and slow modes ( $E_0(k_{\perp})$ ); again, except for the runs with the highest Froude number ( $Fr = 0.32$  and  $Fr = 0.16$ , not shown) and, therefore, buoyancy Reynolds number, the slow

modes dominate at all horizontal scales after the peak of enstrophy. In all cases, the perpendicular spectrum of the slow modes undergoes a growth of energy in horizontal scales larger than the forcing scale (note, however, that since the forcing acts on a spherical shell in Fourier space, there is some injection of energy at all the horizontal scales such that  $0 \leq k_{\perp} \leq k_F$ ). As for the isotropic spectrum, this growth appears to be self-similar for  $N/f$  ratios smaller than 10. As  $N/f$  increases, the perpendicular spectrum saturates at large horizontal scales; see for instance the purely stratified case in figure 8. The spectral slope in this range varies depending on the non-dimensional parameters, and it is difficult to provide precise values here. Nevertheless, it appears that the perpendicular spectrum becomes shallower as  $N/f$  increases. The spectral index  $\alpha_{\perp}$ , defined by  $E_0(k_{\perp}) \sim k_{\perp}^{\alpha_{\perp}}$  for  $k_{\perp} \leq k_F$ , and computed numerically by a least-squares fit, is represented as a function of  $N/f$  in figure 10. The caveats mentioned above regarding accuracy of this spectral index still apply here. For instance, a slightly steeper spectral slope might have been obtained in the purely stratified case if we had chosen a range of wavenumbers closer to the forcing wavenumber: Marino *et al.* (2014) find that the kinetic energy (here we are showing the slow mode energy) has a  $-5/3$  slope in this range. The perpendicular wave spectrum differs markedly in the rotation-dominated, weakly stratified case and in the strongly stratified cases. In the former case, more energy remains at small horizontal scales, while in the latter case it falls off sharply at scales smaller than the forcing scales, and it is shallow or flat at scales larger than the forcing scales. Note that steep horizontal spectra such as those we observe at scales smaller than the forcing scale have been reported before and related to viscous effects (Laval, McWilliams & Dubrulle 2003; Brethouwer *et al.* 2007).

Similarly, the parallel spectra  $E_W(k_{\parallel}), E_0(k_{\parallel})$  of energy in the wave and slow modes, respectively, are shown in figure 9. Again, once the turbulence sets in, the slow modes dominate at all vertical scales, except in the two cases with high buoyancy Reynolds numbers, where the waves dominate at small scales (for the case  $N/f = 1/4$ , the waves dominate roughly at all the vertical scales smaller than the forcing scale  $k_F$ , although the energy in these scales decay extremely fast). Overall, the energy in the small scales increases as we move from the rotation-dominated case (where the spectrum is very steep) to the purely stratified case (note the different vertical scales on the panels of figure 9). This statement also holds for the wave component of the energy: while the waves have most of their energy at large scales for rotation-dominated cases or cases where rotation and stratification are comparable (i.e. relatively low  $N/f$  ratios), they become mostly small scale when stratification prevails. The build-up of slow mode energy at large vertical scales occurs differently from the perpendicular spectra: already at very large times, the parallel spectrum of the slow modes is more or less flat at scales larger than the forcing scale. Besides, for the lowest  $N/f$  ratio (1/4), there is relatively little change in the slow mode parallel spectrum at large scales. As for the perpendicular spectra, there does not seem to be a universal scaling law in this range: the spectral slope  $\alpha_{\parallel}$  (defined by  $E_0(k_{\parallel}) \sim k_{\parallel}^{\alpha_{\parallel}}$  for  $k_{\parallel} \leq k_F$ ) varies between approximately  $-2$  and  $-5/3$  until  $N/f = 4$  (see figure 10), then the spectrum becomes much shallower at large scales, and it is almost flat for the purely stratified case and for the case with  $N/f = 20$ . Note that shallow or flat vertical spectra (and steep horizontal spectra) have been observed in previous studies (e.g. Waite & Bartello 2004), and is associated with rapid decay of vertical velocity correlation functions due to the decoupling of horizontal layers in the limit of strong stratification. Unlike previous studies, this behaviour occurs here for scales larger than the forcing scale. Hence a possible interpretation of the non-universal large-scale vertical spectrum is

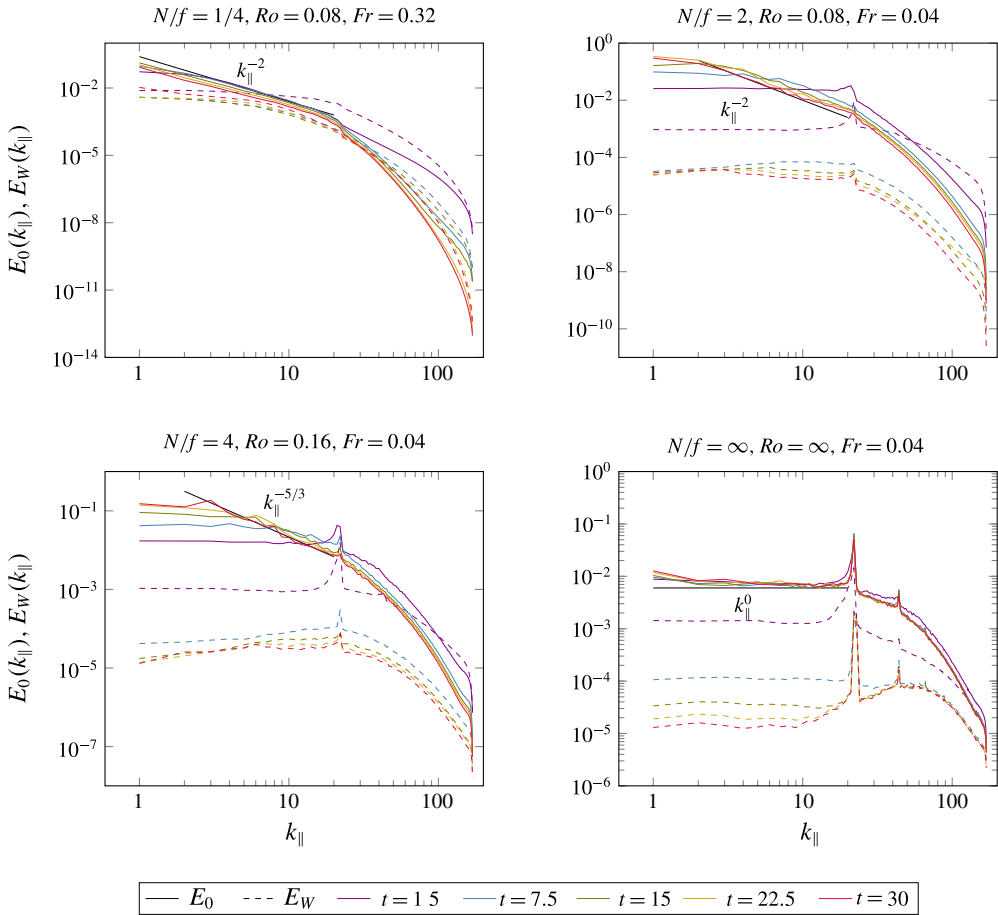


FIGURE 9. (Colour online) Parallel spectra of the wave and slow mode components of energy for selected values of the parameters. Scaling laws are represented only for reference. Line encoding and colours are similar to the three preceding figures.

that it results from a competition between the scrambling effect of the forcing and the build-up of large-scale vertical correlations by inertial effects when rotation is strong enough.

#### 4.3. Role of the VSHF modes

Several studies of stratified flows have underlined the role of horizontally homogeneous modes: Herring & Métais (1989) and Staquet & Godeferd (1998) have reported a tendency towards layering, while Smith & Waleffe (2002, see also Godeferd & Cambon (1994) for an EDQNM perspective) have shown that at very long time, energy accumulates in the horizontally homogeneous modes (defined by  $k_{\perp} = 0$ ), with a peak at some value of  $k_{\parallel}$  which defines the number of horizontal layers in the vertical, hence the name vertically sheared horizontal flows (VSHF). Our numerical simulations are stopped earlier in order to avoid the accumulation of energy in the gravest mode of the system that is inherent to all inverse cascade phenomena (see e.g. Boffetta & Ecke (2012) for a recent review in 2D). Asymptotic analysis has also

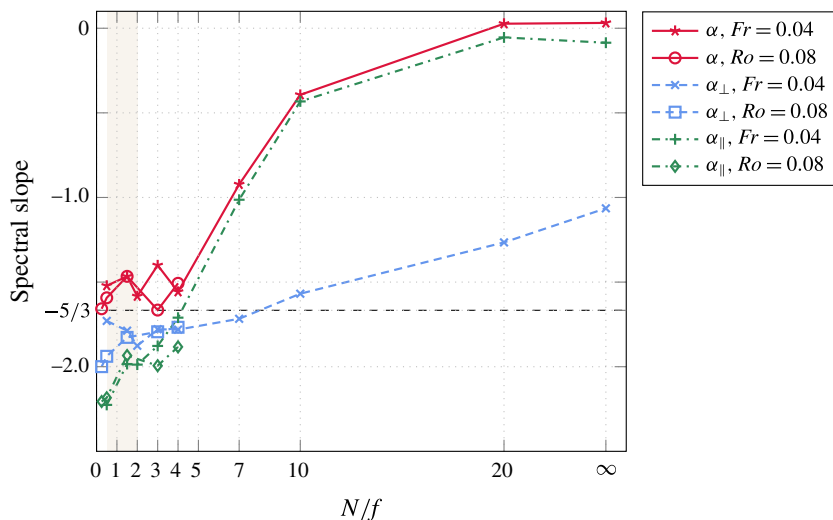


FIGURE 10. (Colour online) Spectral indices for the isotropic (solid lines), perpendicular (dashed lines) and parallel (dash-dotted lines) vortical energy spectra at scales larger than the forcing, as a function of  $N/f$ , for the two series of runs: constant Froude number (star,  $\times$  and  $+$  symbols), and constant Rossby number (circle, square and diamond symbols). The no-resonance zone is the shaded area.

established that the VSHF modes contribute to the slow component of the limiting dynamics in the low-Froude-number, finite-Rossby-number limit (Babin *et al.* 1997; Embid & Majda 1998). This provides an incentive for looking at these modes in the direct numerical simulations carried out here.

By definition, the VSHF modes are horizontally homogeneous, but may depend on the vertical coordinate. In general, they have an inertial wave component (whose frequency is the Coriolis frequency  $f$ ) corresponding to an oscillation of the horizontal components of velocity, with vanishing vertical velocity, and a slow mode component that is proportional to temperature fluctuations. Hence, their wave component is purely kinetic and their slow mode component is purely potential. When rotation vanishes, the dispersion relation also vanishes and there is no longer an oscillatory component.

The ratio of energy in these VSHF modes is shown in figure 11, as a function of  $N/f$  for the two series of runs. It is striking that it remains of the same order of magnitude (and relatively small; it is in fact negligible compared to the waves for instance, see figure 5) for all finite values of  $N/f$ ; it is only when we move to the strictly non-rotating case that the energy in the VSHF modes jumps by approximately two orders of magnitude. Then, the energy in the  $k_{\perp} = 0$  modes becomes comparable to the energy in waves with any other wave vector. Smith & Waleffe (2002) and Waite & Bartello (2006b) also observed an increase of the energy transfer to the VSHF modes when rotation decreases, but here the transition seems to be more abrupt, and the energy fraction in the VSHF modes is also at least an order of magnitude smaller here. However, energy transfers to the VSHF modes is known to occur on very long time scales, and this may simply be a matter of integration time.

Note that, although we do not have enough runs at high buoyancy Reynolds number for a systematic study, it does not seem to be a relevant parameter as far as this issue is concerned, since the two runs with higher buoyancy Reynolds have a similar level of energy in the VSHF modes as the other runs.

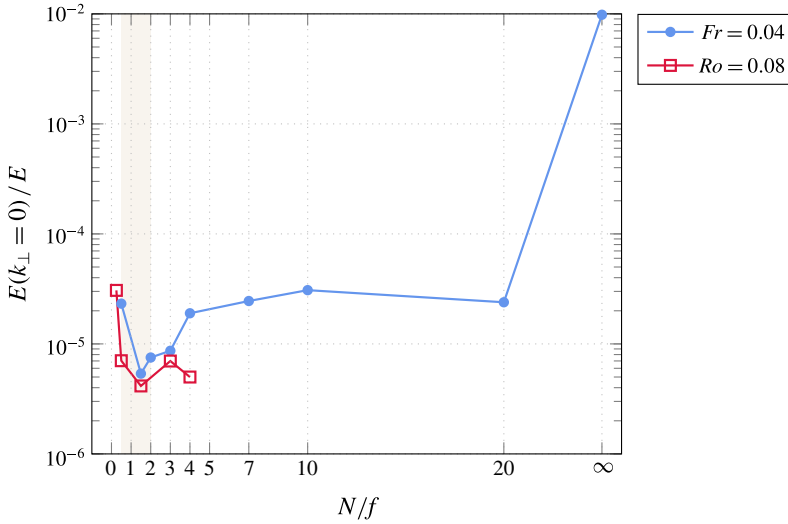


FIGURE 11. (Colour online) Fraction of energy in the vertically sheared horizontal modes ( $k_{\perp} = 0$  modes) as a function of  $N/f$ , for the two series of runs. The no-resonance zone is the shaded area.

#### 4.4. Energy fluxes

Let us now turn to the fluxes of energy in the different modes. We first define the transfer functions  $T_0(\mathbf{k})$  and  $T_W(\mathbf{k})$ :

$$T_0(\mathbf{k}) = \text{Re} \left[ X_0(\mathbf{k})^\dagger \sum_{\mathbf{p}+\mathbf{q}=\mathbf{k}} ik^j \hat{u}_j(\mathbf{p}) X(\mathbf{q}) \right], \tag{4.5}$$

$$T_W(\mathbf{k}) = \text{Re} \left[ X_W(\mathbf{k})^\dagger \sum_{\mathbf{p}+\mathbf{q}=\mathbf{k}} ik^j \hat{u}_j(\mathbf{p}) X(\mathbf{q}) \right], \tag{4.6}$$

where we have introduced the projections  $X_0(\mathbf{k}) = \mathbf{P}_0(\mathbf{k})X(\mathbf{k})$  and  $X_W(\mathbf{k}) = \mathbf{P}_W(\mathbf{k})X(\mathbf{k})$ . The evolution of the energy in the slow and wave modes at wave vector  $\mathbf{k}$  is simply governed by

$$(\partial_t + 2\nu k^2)E_0(\mathbf{k}) = T_0(\mathbf{k}), \tag{4.7}$$

$$(\partial_t + 2\nu k^2)E_W(\mathbf{k}) = T_W(\mathbf{k}). \tag{4.8}$$

As usual, we can define the isotropic, perpendicular and parallel transfer functions  $T_s(k)$ ,  $T_s(k_{\perp})$  and  $T_s(k_{\parallel})$  (with  $s = 0, W$ ) by integrating over a spherical shell, a plane or a cylinder in Fourier space. Then we introduce the fluxes:

$$\Pi_0(k) = \int_k^{k_{max}} T_0(k) dk, \tag{4.9}$$

$$\Pi_W(k) = \int_k^{k_{max}} T_W(k) dk, \tag{4.10}$$

and similarly for the perpendicular and parallel fluxes  $\Pi_s(k_{\perp})$  and  $\Pi_s(k_{\parallel})$ .



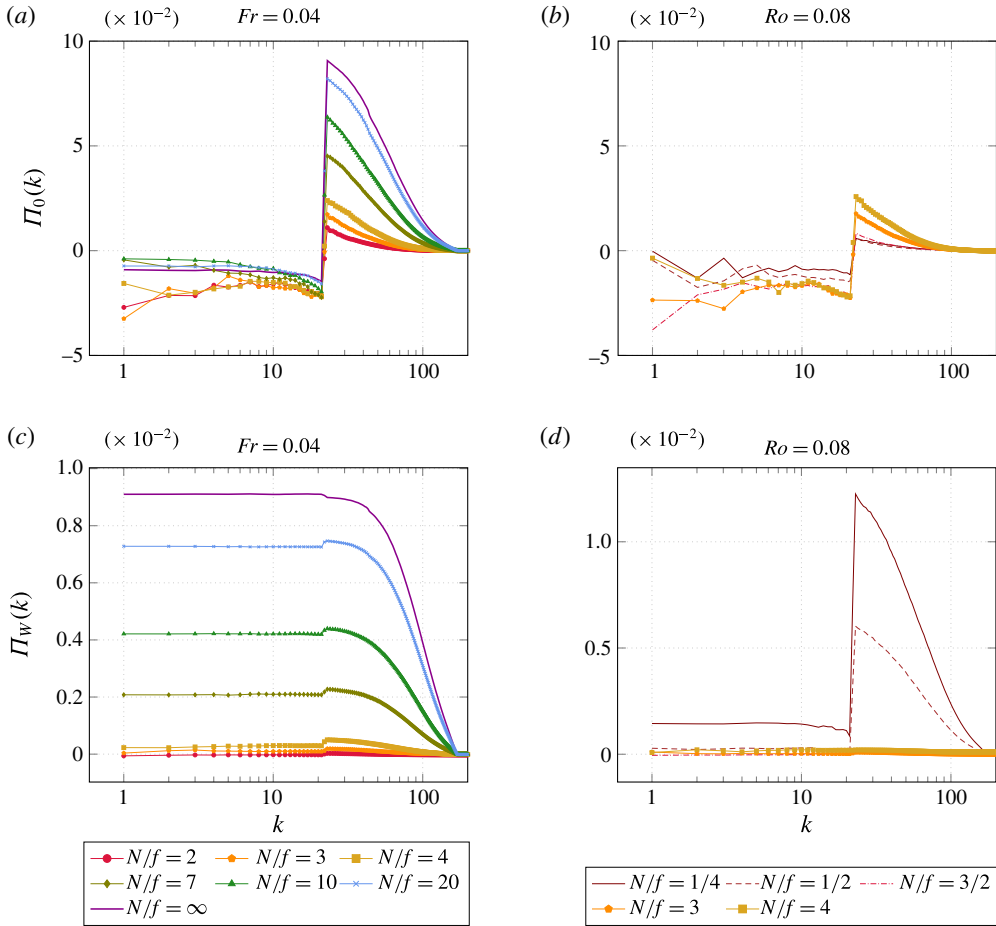


FIGURE 12. (Colour online) Isotropic fluxes of energy for the slow modes (a,b) and for the wave modes (c,d) for the series of runs at constant Froude number (a,c) and at constant Rossby number (b,d) with various  $N/f$ . Note the different scale (they differ by a factor of 10) for  $\Pi_0$  and  $\Pi_W$ .

The isotropic energy fluxes for the slow modes and for the waves are shown in figure 12 for the latest time ( $t = 30$ ). We see that for all  $N/f$  ratios, the energy fluxes for the slow modes are negative, and more or less independent of  $k$ , at scales larger than the forcing. Furthermore, the magnitude of this negative flux seems to be larger for relatively small values of  $N/f$  (the runs with  $N/f = 2, 3, 4$  have approximately the same magnitude), while it is reduced when stratification prevails. In contrast, the fluxes are positive at scales smaller than the forcing. In this range, the positive flux is an increasing function of  $N/f$ . On the other hand, the energy fluxes for the wave modes do not change sign at the forcing scale: they are always positive. The absence of a range with constant small-scale fluxes can be attributed to the small size of the  $k > k_F$  wavenumber range, a problem remedied when using higher resolutions and/or lower forcing wavenumber (Pouquet & Marino 2013; Marino, Pouquet & Rosenberg 2015), or a parametrization scheme (Pouquet *et al.* 2013). Note that, unlike the traditional (total) energy fluxes, we need not have  $\Pi_s(0) = 0$ , because  $E_0$  and  $E_W$

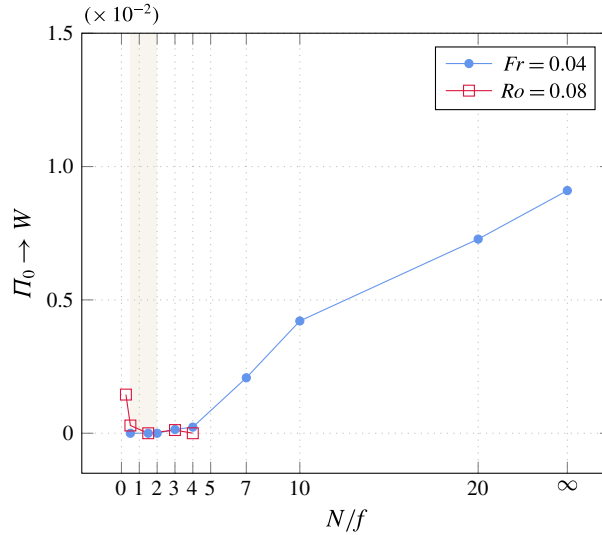


FIGURE 13. (Colour online) Total energy flux from the slow modes to the wave modes as a function of  $N/f$ .

are not independently conserved (only their sum is). This means that care should be taken when interpreting fluxes, since the value of the flux for one given mode (slow or wave) at  $k$  is not only the amount of energy transferred from wavenumbers smaller than  $k$  to wavenumbers larger than  $k$ , but also includes the contributions from the other mode. The total flux of energy from the slow modes to the waves  $\Pi_{0 \rightarrow w}$ , which coincides with  $\Pi_w(0)$ , or equivalently  $-\Pi_0(0)$  (up to numerical errors), is shown as a function of  $N/f$  in figure 13. Such global energy exchanges between slow and fast modes have been considered in more details (including the partition of energy into kinetic and potential components) by Whitehead & Wingate (2014); here we use the global flux to interpret the spectral distribution of the energy fluxes.  $\Pi_{0 \rightarrow w}$  is small when  $N/f$  is small (up to  $N/f = 4$ ) and then increases almost linearly with  $N/f$ . For all values of  $N/f$  larger than unity, the energy flux for the wave modes (figure 12) is never significantly larger than  $\Pi_{0 \rightarrow w}$ , which means that the transfer of wave energy is dominated by the leakage from slow modes. However, note that for the two cases  $N/f = 1/4$  and  $N/f = 1/2$ , the flux at scales smaller than the forcing scale is much larger than  $\Pi_{0 \rightarrow w}$ , meaning that, in those cases, there is a significant transfer of energy towards the small scales from the waves themselves. This interpretation is consistent with the fact that in the  $N/f = 1/4$  case the energy in the wave modes is significantly larger than in any other case, and these two cases are those for which the waves dominate at small scales (see figure 7), and for which the buoyancy Reynolds number is significantly larger. Similarly, the negative flux at scales larger than the forcing scales for the slow modes is of the order of  $\Pi_{0 \rightarrow w}$  when  $N/f \geq 7$ . This means that the negative flux alone does not allow one to claim with certainty that we have an inverse cascade of slow modes. For instance, slow energy in the stratified case has a negative flux, while we have seen above that it lacks some characteristics of the inverse cascade. What is more meaningful is the fact that, in the range of scales between the forcing scale and the plateau of the flux at the largest scales, the flux decreases with  $k$  and goes below the level of  $\Pi_{0 \rightarrow w}$ , all the more so that  $N/f$  is small, consistently with the above analysis.

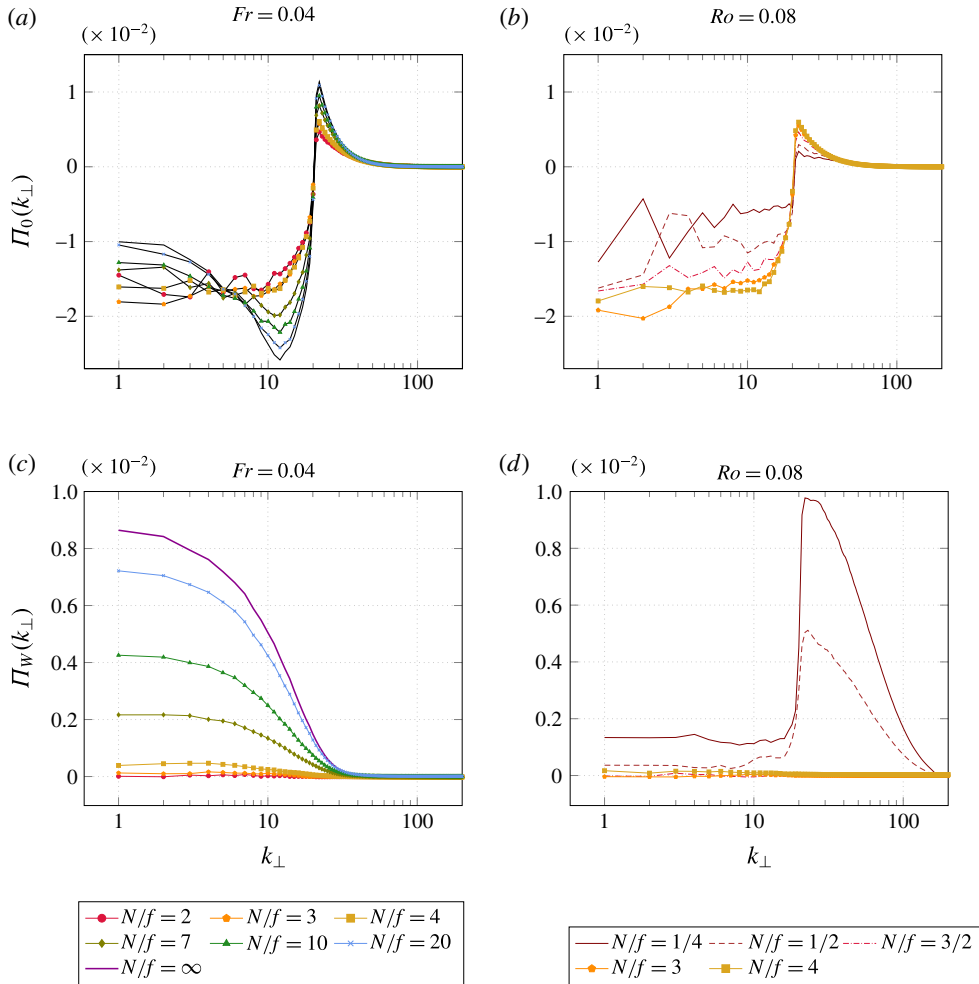


FIGURE 14. (Colour online) Perpendicular fluxes of energy for the slow modes (a,b) and for the wave modes (c,d) for the series of runs at constant Froude number (a,c) and constant Rossby number (b,d) with various  $N/f$ .

For the runs with  $N/f \leq 4$ , the interpretation of the negative flux of slow energy is much easier: the magnitude of the more or less constant flux over scales larger than the forcing scales is much larger than  $\Pi_{0 \rightarrow w}$ , which means that it can safely be attributed to an inverse cascade of slow mode energy.

In figure 14, we show the perpendicular fluxes of energy in the slow modes and in the waves,  $\Pi_0(k_\perp)$  and  $\Pi_w(k_\perp)$ . For the slow modes, the fluxes are similar to the isotropic fluxes, with a notable difference: the negative fluxes at scales larger than the forcing scale are enhanced. In particular, now all the runs have a wide range of scales (larger than the forcing scale) for which the flux has larger magnitude than  $\Pi_{0 \rightarrow w}$ . That means that, regardless of  $N/f$ , slow mode energy tends to be transferred towards large horizontal scales. This is known to be true even for purely stratified flows or flows strongly dominated by rotation, which tend to form uniform layers (Riley & Lelong 2000). As a matter of fact, runs dominated by stratification have

a (negative) peak in the slow mode energy flux whose magnitude increases with  $N/f$ . The fluxes indicate, however, that for stratification-dominated runs (e.g.  $N/f = 20$  or  $\infty$ ), this transfer of slow energy is arrested at some horizontal scales (like kinetic energy; see Marino *et al.* 2014), while it continues all the way to the largest scales when stratification is weaker (e.g.  $N/f = 2, 3, 4$  or even 7 and 10). In contrast, the energy fluxes in the wave modes are always smaller than  $\Pi_{0 \rightarrow W}$  and, contrary to the isotropic fluxes, they do not have any range of constant value. This indicates that the transfer of energy from the slow modes to the waves probably occurs at large horizontal scales (we cannot in principle draw definitive conclusions since there might be cancellations between energy transfer from slow to wave modes and transfer across scales of wave modes, but it does not seem very plausible that they are of different signs). Note that the forcing scale is difficult to identify from this figure alone. It should be emphasized that, since we are forcing in a spherical shell in Fourier space, energy is actually injected in the full range  $k_{\perp} \in [0, k_F]$  (the same goes for  $k_{\parallel}$  of course). Hence a caveat in the interpretation of anisotropic fluxes is that the forcing scale is not so well defined. However, in almost all cases, except the above-mentioned, the forcing scale can still be identified unambiguously in  $\Pi_s(k_{\perp})$  and  $\Pi_s(k_{\parallel})$ , which gives us confidence that the forcing is not contaminating the results too much. Finally, the perpendicular fluxes of wave energy for the two cases  $N/f = 1/4$  and  $N/f = 1/2$  are very similar to the isotropic fluxes, which means that, in those cases, the near-inertial waves tend to transfer their energy towards small horizontal scales.

Now, we turn to the examination of the parallel flux of energy in the slow modes and in the wave modes (figure 15). The most notable results are that runs with  $N/f \geq 7$  have positive fluxes of slow energy across the whole range of vertical scales, corresponding to the maintenance of horizontal layers, whose thickness decreases with  $N/f$ . This process is less clear when stratification is weaker, since the parallel flux then remains negative at the very large scales. For all the runs with  $N/f \geq 2$ , the parallel flux of wave energy is identical to the isotropic flux, indicating that vertical transfers dominate, although interpretation is still polluted by the exchange with slow modes. When  $N/f = 1/4$  or  $N/f = 1/2$ , it is interesting to note that there is a peak at vertical scales larger than the forcing scale (this is another case where the isotropic forcing scale does not appear clearly), although its magnitude is relatively small. This peak does not correspond to any identifiable feature in the isotropic fluxes.

## 5. Viscous dissipation due to vertical shearing and the role of the buoyancy Reynolds number

### 5.1. Impact of viscous effects on spectral energy budgets

As mentioned in § 2.2, the non-dimensional parameters characterizing the numerical simulations being studied here correspond to a regime where vertical diffusion terms are of the order of vertical advection (Billant & Chomaz 2001; Godoy-Diana, Chomaz & Billant 2004; Brethouwer *et al.* 2007). In this regime, viscous dissipation can affect the large horizontal scales through vertical shearing of the layers (the so-called ‘pancakes’) formed by the dynamics. Following the work of Brethouwer *et al.* (2007) – see their (4.1) and figure 10 – for purely stratified flows, we check this effect explicitly by considering the ratio of the dissipation due to vertical shear  $\epsilon_S$  to the total dissipation  $\epsilon$ . These two quantities are given by:

$$\epsilon_S = \nu \int [(\partial_z u_x)^2 + (\partial_z u_y)^2], \quad (5.1)$$

$$\epsilon = \nu \int (\partial_i u_j)(\partial^i u^j). \quad (5.2)$$

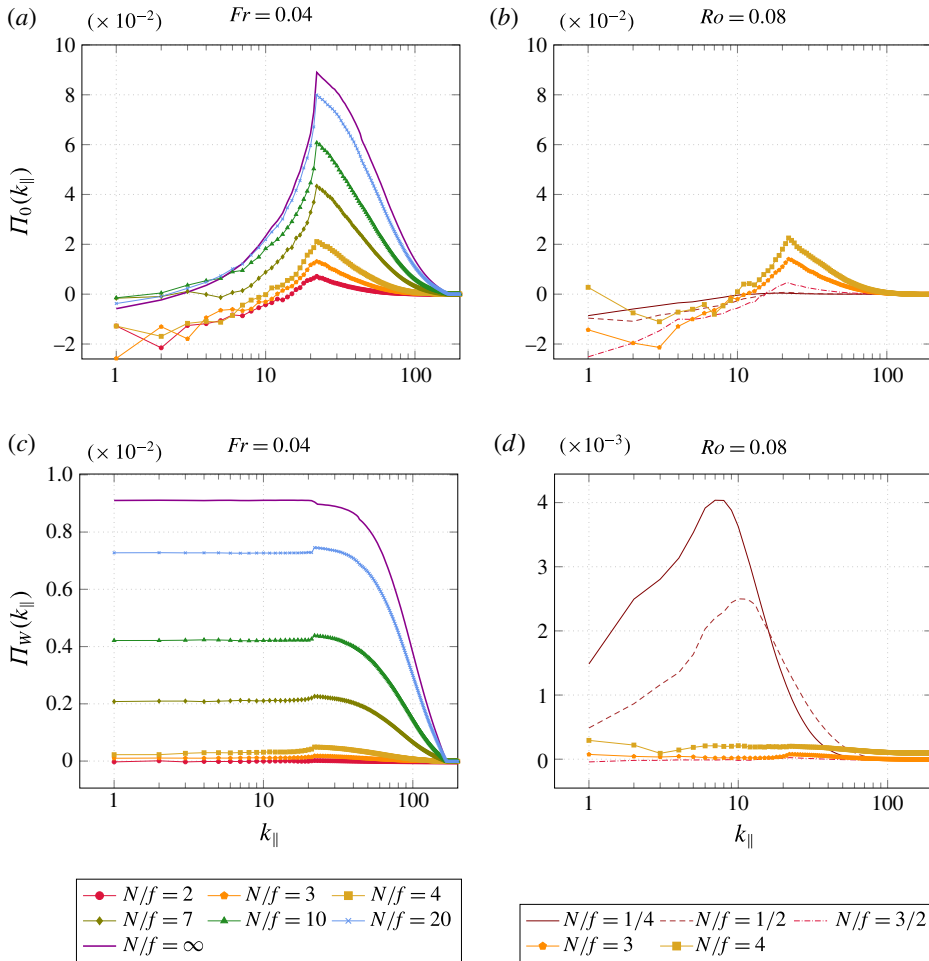


FIGURE 15. (Colour online) Parallel fluxes of energy for the slow modes (a,b) and for the wave modes (c,d) for the series of runs at constant Froude number (a,c) and at constant Rossby number (b,d) with various  $N/f$ .

The ratio  $\epsilon_S/\epsilon$  is represented as a function of  $N/f$  in figure 16, for both series of runs. For low  $N/f$ , this ratio is very small and, as expected, it increases when thinner horizontal layers form which allow vertical dissipation to act, until reaching values for  $N/f = 20$  or  $N/f = \infty$  similar to the stratified runs of Brethouwer *et al.* (2007) at similar  $\mathcal{R}_B$ , for which the major part of dissipation is due to these large-scale viscous effects.

Now, we would like to know what part this large-scale dissipation mechanism potentially plays in preventing the energy transfers towards the large scales when  $N/f$  varies. To do so, we would like to compare the dissipation rate in a given range of scales to the flux of energy transferred by the nonlinear term in the same range. Hence, we introduce the following integrals of the viscous term:

$$D_<(k) = 2\nu \int_0^k p^2 E(p) dp, \quad D_>(k) = 2\nu \int_k^{k_{max}} p^2 E(p) dp, \quad (5.3a,b)$$

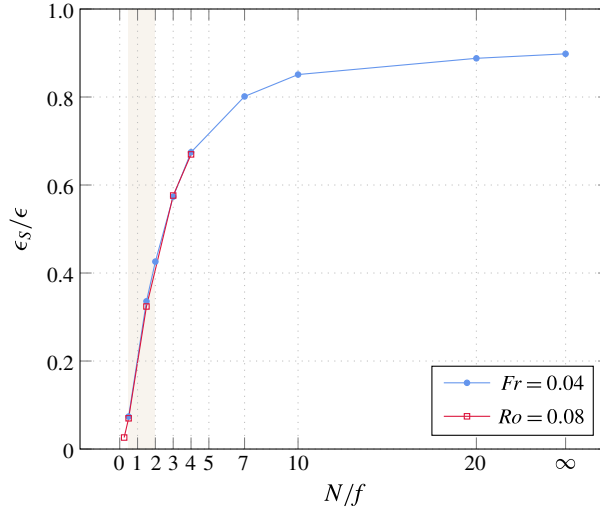


FIGURE 16. (Colour online) Fraction of the kinetic energy dissipation rate due to vertical shearing of the horizontal velocity field.

$$D_{<}(k_{\perp}) = 2\nu \int_{p_{\perp} \leq k_{\perp}} p^2 E(\mathbf{p}) \, d\mathbf{p}, \quad D_{>}(k_{\perp}) = 2\nu \int_{p_{\perp} \geq k_{\perp}} p^2 E(\mathbf{p}) \, d\mathbf{p}, \quad (5.4a,b)$$

$$D_{<}(k_{\parallel}) = 2\nu \int_{p_{\parallel} \leq k_{\parallel}} p^2 E(\mathbf{p}) \, d\mathbf{p}, \quad D_{>}(k_{\parallel}) = 2\nu \int_{p_{\parallel} \geq k_{\parallel}} p^2 E(\mathbf{p}) \, d\mathbf{p}, \quad (5.5a,b)$$

and we similarly define the fluxes  $\Pi_{<}, \Pi_{>}$  by integrating the transfer functions. Note that  $\Pi_{<} = -\Pi_{>}$  (because the integral of the transfer functions over all wave vectors vanishes), but of course there is no analogous property for the dissipation term, which is positive definite. Now we can write integrated energy budgets for large and small scales:

$$\frac{d}{dt} \int_0^k E(p) \, dp = \Pi_{<}(k) - D_{<}(k) \quad \text{for } k < k_f, \quad (5.6)$$

$$\frac{d}{dt} \int_k^{k_{max}} E(p) \, dp = \Pi_{>}(k) - D_{>}(k) \quad \text{for } k > k_f. \quad (5.7)$$

We can proceed analogously for the perpendicular and the parallel directions, with the caveat that, for the type of forcing considered here, there is an additional energy injection term in the large-scale budget, due to the projection of the forcing term in the spherical shell of radius  $k_f$  on horizontal and vertical wavenumbers in the interval  $[0, k_f]$ . In figure 17, we show the two terms on the right-hand side of the large-scale energy budget, for isotropic and horizontal scales, for the four highest values of  $N/f$ . For isotropic scales larger than the forcing scale, the small flux of energy towards large scale which exists near  $k_f$  in the purely stratified case is annihilated by dissipation. As  $N/f$  decreases, both the value of the flux of energy towards large scales and the range where it is positive grow, as has already been reported (Marino *et al.* 2013, 2014). In addition, the difference between the energy flux and dissipation also grows at all scales  $k < k_f$ , although the large-scale energy

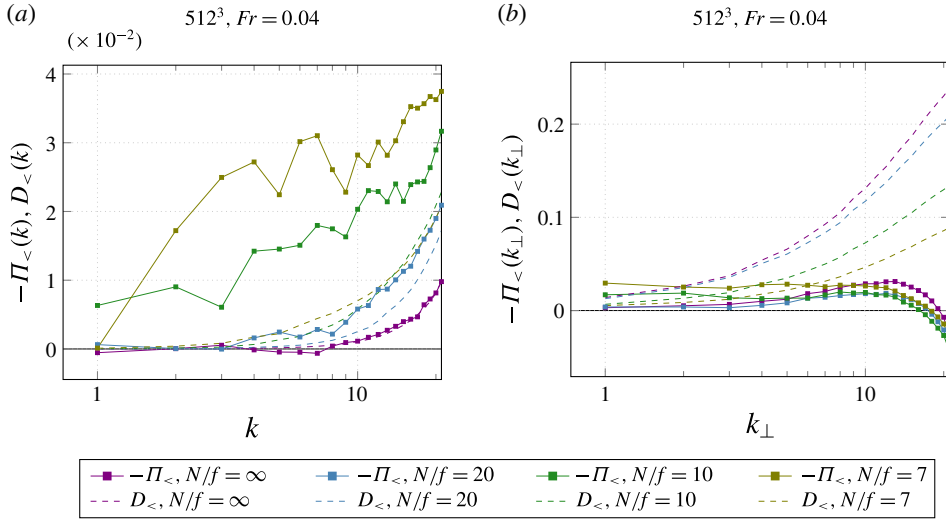


FIGURE 17. (Colour online) Isotropic (a) and perpendicular (b) fluxes of kinetic energy into the large scales (solid lines),  $-\Pi_{<}(k)$  and  $-\Pi_{<}(k_{\perp})$ , respectively, and rate of kinetic energy dissipation by viscosity at large scales (dashed lines),  $D_{<}(k)$  and  $D_{<}(k_{\perp})$ , respectively. Only the scales larger than the forcing scale are shown. Note the different vertical scale for the two plots.

dissipation itself increases when  $N/f$  decreases. This shows that, in the parameter regime considered here ( $\mathcal{R}_B \sim 1$ ), the disappearance of the inverse cascade when  $N/f$  increases is due to the combination of two effects. First of all, the nonlinear term does not transfer energy to the large scale as efficiently. Besides, the small amount of energy which is still transferred to large isotropic scales is damped by viscous dissipation due to vertical shearing. The situation is slightly different when considering perpendicular scales. While the behaviour of the energy flux when  $N/f$  varies as been described above, the energy dissipation at large horizontal scales increases with  $N/f$ , for all  $k_{\perp} < k_f$  and more markedly for  $k_{\perp}$  closer to  $k_f$ . It should be noted that for stratification-dominated flows (here the runs with  $N/f = 20$  or  $\infty$  for instance), dissipation is larger than energy flux at all horizontal scales larger than the forcing scale. As  $N/f$  decreases, the energy flux starts prevailing at the largest scales, and the crossing scale decreases with  $N/f$ . This explains how the blob in the energy flux towards large horizontal scales in the stratified case does not lead to accumulation of energy at large scales.

The integrated budget for large parallel scales (not shown) exhibits yet another scenario: there, nonlinear transfer and viscous dissipation act together to remove energy from large parallel scales. The source of energy at  $k_{\parallel} < k_f$  is the projection of the forcing, and the major part of this input is transferred towards small vertical scales by the nonlinear term, the remaining energy being damped by viscosity. The ratio of the energy flux towards small vertical scales and the viscous dissipation increases as  $N/f$  increases, indicating the trend for stratification-dominated flows to form thinner layers.

In all the runs considered here, the small-scale integrated energy budget exhibits an exact balance between nonlinear energy transfers and dissipation (not shown), in agreement with the fact that those scales are in a steady state. This holds for isotropic, perpendicular and parallel scales alike.

### 5.2. Impact of the buoyancy Reynolds number

As pointed out by several authors (Brethouwer *et al.* 2007; Ivey, Winters & Koseff 2008; Bartello & Tobias 2013; Waite 2013), the buoyancy Reynolds number  $\mathcal{R}_B$  plays an important role in stratified turbulence, and it is likely doing so as well when rotation is included. In particular, the regime of low buoyancy Reynolds number corresponds to a case where horizontal layers are viscously coupled. It is characterized by a vertical scale set by the viscous scale  $\sqrt{\nu L_h/U}$  rather than the buoyancy scale  $U/N$  (Riley & de Bruyn Kops 2003; Godoy-Diana *et al.* 2004; Brethouwer *et al.* 2007; Rorai *et al.* 2014), a small vertical Froude number (in contrast, at high buoyancy Reynolds number, the vertical Froude number remains of order unity (Billant & Chomaz 2001)) and a potential enstrophy which is dominated by its quadratic component (Waite 2013). The runs commented upon so far fall within this parameter regime and, as explained in the previous section, viscous dissipation due to vertical shearing has to be taken into account to understand the energy budget, even at large (horizontal) scales. Nevertheless, the results presented here tend to show that in this regime, the system relaxes to a balanced state where the velocity field is almost horizontal (the slow modes have vanishing vertical velocity), and slow mode energy is cascaded upscale provided rotation is strong enough.

It is a natural question to ask how both the inertial and viscous mechanisms outlined above, which account for the collapse of the inverse cascade when  $N/f$  increases, are affected when the buoyancy Reynolds number moves closer to a regime relevant for geophysical flows. One expects that when  $\mathcal{R}_B$  becomes large, the viscous effects should disappear, the non-quadratic components of potential enstrophy will grow and the transfer of energy to the waves will also be larger. However, it remains unclear whether these transitions all occur at the same time or if some of those effects vanish before the others. A systematic study of the effect of the buoyancy Reynolds number across a wide range of  $N/f$  such as the one studied here would be extremely expensive computationally speaking. Indeed, two incompatible conditions are required: on the one hand a reasonable scale separation between the forcing scale and the box scale is needed to discuss the inverse cascade regime, which reduces the Reynolds number, but on the other hand a very large Reynolds number is needed to reach a high  $\mathcal{R}_B$ . In addition, the option of decreasing the forcing wavenumber suffers from another limit: in the purely stratified case, when  $k_F$  is too low, we observe an accumulation of energy at the forcing scale. A possible explanation for this behaviour is that the number of modes excited does not suffice to spread the energy across the whole spectrum of scales.

To get a rough idea of how the results obtained above in the low  $\mathcal{R}_B$  regime change when  $\mathcal{R}_B$  increases, we have carried out four additional simulations (see table 1). One purely stratified run and one with  $N/f = 20$  were carried out at  $512^3$  resolution and  $k_F = 11$ . The last two have a  $1024^3$  resolution and  $k_F = 22$ , again with  $N/f = 20$  or  $\infty$ . In all these cases, the buoyancy Reynolds number is twice the value of the original runs.

Many features of these runs are similar to the ones already analysed. In particular, the isotropic and parallel spectra are all more or less flat at scales larger than the forcing scale. However, there are also notable differences. First of all, run F'20 undergoes a linear growth of slow energy, unlike run F20. However, this growth of energy does not correspond to a self-similar growth of the spectrum, which remains relatively shallow. The purely stratified runs F\*20 and F\*\infty both exhibit a slow decay of slow energy and a corresponding growth of wave energy, which ultimately dominates at the latest stages of run F\*20, indicating that the transfer



of energy towards waves is much larger at larger  $\mathcal{R}_B$ . Besides, in all the runs and as anticipated above, waves dominate at small scales, especially at small horizontal scales. Regarding potential vorticity,  $\Gamma_2/\Gamma$  is approximately 0.975 in the  $N/f = 20$  case, a value which is close to that observed in figure 2. In the purely stratified case, this ratio is around 0.92 and keeps increasing slowly in time until the end of the run. The run with  $k_F = 11$  and the  $1024^3$  run agree reasonably well on this value, which is slightly lower than in the low- $\mathcal{R}_B$  case (see figure 2). Perhaps the most interesting thing to compare with the low- $\mathcal{R}_B$  runs is the large-scale energy budget as described in § 5.2. It is represented in figure 18. While the effect of large-scale dissipation is as expected slightly lower than in the lower- $\mathcal{R}_B$  case, the most notable difference is in the nonlinear energy transfer. Indeed, in the purely stratified case, the contribution of the nonlinear term to the energy budget of the (isotropic) scales larger than the forcing scale is negative, at variance with the lower- $\mathcal{R}_B$  case. It is slightly smaller (though still positive when  $N/f = \infty$ ) when looking at the horizontal scales, and becomes negative for  $k_\perp$  closer to  $k_F$  when  $N/f = 20$ . In the case  $N/f = 20$ , the nonlinear energy transfers overcome viscous dissipation in the isotropic large-scale budget. This explains the linear growth of energy mentioned above.

## 6. Conclusion

We have studied the partition of energy in terms of waves and vortices, defined through the normal modes of the linearized equations, in stratified flows with or without rotation. We have focused on the inverse cascade regime, which appears when rotation is sufficiently strong but not when stratification dominates. Using numerical simulations covering a wide range of  $N/f$  ratios, we have characterized this transition in terms of the waves and vortices. To sum up, §§ 4.1–4.4 have established that in all the runs shown here:

- (i) The total energy is dominated by the slow mode component, even when stratification is strong, although the fraction of energy in the waves increases when  $N/f \geq 2$  increases. This happens in spite of the fact that the forcing has roughly equal projections on the slow and wave modes. The increase in wave energy with  $N/f$  is consistent with the observed total flux of energy from the slow modes to the wave modes, which also increases with  $N/f$ .
- (ii) The slow mode component dominates at all scales, except in the two runs with higher buoyancy Reynolds number (those with  $N/f = 1/4$  and  $1/2$ ), where they only dominate at large scale, similarly to the large-scale forcing case (Sukhatme & Smith 2008; Kurien & Smith 2012, 2014). This also holds when distinguishing horizontal and vertical scales.
- (iii) When  $N/f$  is small enough (roughly  $N/f \leq 7$ , although the specific value may depend on the details of the set-up, and, in particular, the buoyancy Reynolds number and the strength of the waves due to rotation and/or stratification), the slow mode component has all the characteristics of an inverse cascade of energy: linear growth of their global energy, self-similar growth of their energy at scales larger than the forcing scales, and negative and constant fluxes at scales larger than the forcing scale. This is consistent with the results obtained in different set-ups in previous studies (Brunner-Suzuki *et al.* 2014; Kurien & Smith 2014; Whitehead & Wingate 2014).
- (iv) When  $N/f$  is higher (here because rotation is decreased), this inverse cascade of slow energy is arrested. When stratification prevails, slow modes still dominate the total energy, and there is some transfer of these modes towards the large

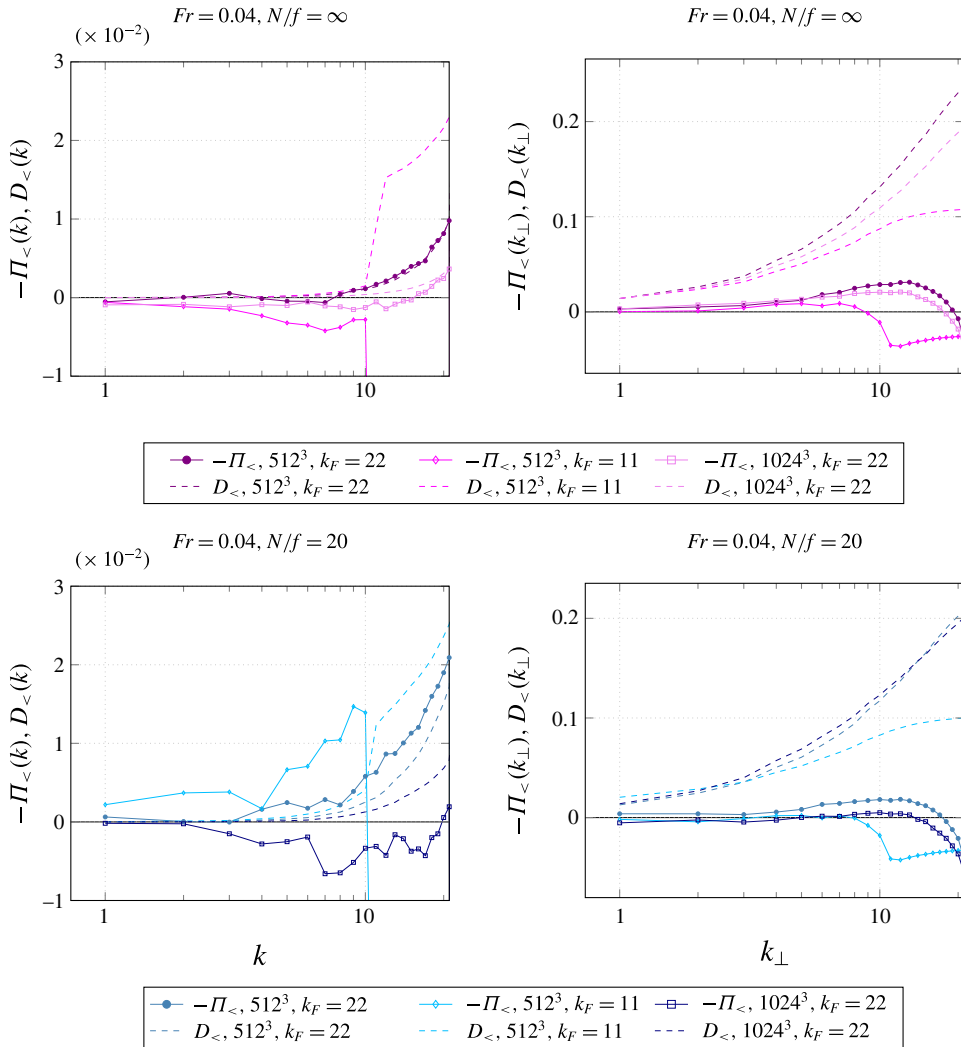


FIGURE 18. (Colour online) Impact of the buoyancy Reynolds number on the large-scale energy budgets. The curves are similar to figure 17.

scales, but it does not take the form of an inverse cascade: it saturates with a flat spectrum at large isotropic and vertical scales (like the full spectrum (Smith & Waleffe 2002; Waite & Bartello 2004; Kimura & Herring 2012)), and there is no significant negative flux of energy for those scales. The spectrum is not flat at large horizontal scales, consistent with the presence of significant negative flux of slow mode energy, but it is still much shallower than in the presence of rotation. Note that the inverse cascade starts vanishing at a value of  $N/f$  for which the deformation scale becomes comparable to the box size. This can be interpreted intuitively as the fact that rotation is not directly felt at any of the resolved scales.

- (v) As long as rotation is present, the fraction of energy in horizontally homogeneous modes (VSHF modes, satisfying  $k_{\perp} = 0$ ) does not vary much with  $N/f$ , and this fraction is always much lower than the energy in the waves, which is itself

much lower than the energy in the slow modes. In contrast, in the purely stratified case, the VSHF modes reach a level of energy comparable with the waves. Interestingly, this transition appears to be pretty sharp, in contrast to all the other properties of the flows we have studied here (e.g. global partition of energy between waves and slow modes, growth rate of the slow mode energy and spectral indices), which seem to have a smoother transition as  $N/f$  increases.

The above results add up to those of Smith & Waleffe (2002) in an effort to better understand the role of vortices and waves in the inverse cascade of rotating-stratified flows, and more generally, to the above-mentioned studies in the wider context of geophysical flows. They also shed light on a paradox regarding the fundamental fluid mechanics of such flows. Indeed, the idea that the inverse cascade observed in the presence of rotation collapses when  $N/f$  increases has been in the literature for a while (Métais *et al.* 1994; Bartello 1995; Lilly *et al.* 1998; Smith & Waleffe 2002; Lindborg 2005; Waite & Bartello 2006b; Aluie & Kurien 2011). However, from a theoretical point of view, this may come as a surprise because the inviscid invariants, which are traditionally reliable indicators of the direction of the energy cascade, are the same regardless of the  $N/f$  ratio (including in the purely stratified case). Here, we have attempted to reconcile these two facts. A major ingredient is that the second invariant (in addition to energy), potential enstrophy, is degenerate. A similar situation occurs in homogeneous isotropic turbulence, where helicity is not sign-definite in general (in our case the sign of potential enstrophy is constant; it vanishes for wave modes and, in the non-rotating case, for VSHF modes). When one decimates the system by keeping only helical modes of a given sign, helicity becomes sign-definite and an inverse cascade results, as observed numerically (Biferale, Musacchio & Toschi 2012) and in agreement with statistical mechanics arguments (Herbert 2014; Zhu, Yang & Zhu 2014). But when one starts reintroducing in the dynamics a fraction of the modes which destroy sign-definiteness of the invariant, the inverse cascade collapses very soon (Sahoo, Bonaccorso & Biferale 2015), which again seems in agreement with the statistical mechanics prediction (Herbert 2014) and the behaviour of purely stratified flows described above. An alternative constraint which leads to the reversal of the energy flux is confinement: when the aspect ratio of the domain is small, enstrophy production is inhibited at scales larger than the layer thickness, even in the presence of stratification (Smith, Chasnov & Waleffe 1996; Celani, Musacchio & Vincenzi 2010; Sozza *et al.* 2015).

Based on the inviscid invariants (Herbert *et al.* 2014), we have identified three inertial mechanisms which can account for the collapse of the inverse cascade of slow modes, and which the numerical simulations proved to be simultaneously at play: first of all, although vortices dominate in all cases, the total flux of energy from slow modes to waves increases as  $N/f$  increases (see figure 13), and consequently the fraction of energy in the waves also increases (see figure 5). Besides, in the purely stratified case, there is an accumulation of energy in the VSHF modes, which do not contribute to quadratic potential enstrophy (see figure 11). Finally, as  $N/f$  increases, the approximation of potential enstrophy by its quadratic part, on which the inviscid invariants argument is based, becomes less and less accurate (see figure 2). In addition to these inertial mechanisms, viscous effects also play a part at low buoyancy Reynolds number: in the purely stratified case, the energy transfer by the nonlinear term towards large scales (in particular horizontal scales) is sufficiently small to be completely dissipated by viscous effects at large horizontal scales due to vertical shearing.

When the buoyancy Reynolds number increases, it is expected that such viscous effects should vanish, but the other mechanisms described above should be affected as well. Our preliminary sensitivity tests give a first indication that, while viscous effects are indeed reduced, the larger transfer of energy towards wave modes (which dominate at small scales) will probably play a major part. This is bound to happen when the Ozmidov scale is resolved, since then isotropy is recovered and there is no longer any reason for the velocity field to be mostly horizontal: since the vertical velocity in the normal mode decomposition framework is entirely accounted for by the wave modes, their contribution has to be larger at these scales. In this regime, the nonlinear components of potential vorticity are also stronger. To add further complication, numerical simulations have shown that in this high- $\mathcal{R}_B$  regime, both an inverse and a direct cascade of energy could exist simultaneously (Pouquet & Marino 2013; Marino *et al.* 2015). From the point of view of the inviscid invariants of the system, this is a puzzling result since inverse cascades usually arise when a second invariant prevents the direct cascade (see § 2.4). The key to this phenomenon presumably also lies in the fact that the energy breaks up into a wave component (not constrained by potential enstrophy conservation) and a vortical component (constrained by potential enstrophy conservation), even though, in this regime, more energy is transferred from the slow modes to the waves. Given that geophysical flows, which are a major motivation for better understanding the role of internal waves and vortices in rotating-stratified flows, fall within this high- $\mathcal{R}_B$  regime, more efforts should be devoted to studying such questions in future research.

### Acknowledgements

The work of C.H. on this research was partially supported by the Advanced Study Program and the Geophysical Turbulence Program at NCAR. The National Center for Atmospheric Research is sponsored by the National Science Foundation. R.M. was supported by the Regional Operative Program, Calabria ESF 2007/2013 and the European Community's Seventh Framework Programme FP7-PEOPLE-2010-IRSES under grant agreement no. 269297 – TURBOPLASMAS. A.P. acknowledges support from the Laboratory for Atmospheric and Space Physics, University of Colorado. D.R. acknowledges support from the Oak Ridge Leadership Computing Facility at ORNL via the Office of Science under DOE Contract no. DE-AC05-00OR22725. Computer time was provided by ASD/ASP (NCAR) and the WEXAC cluster (Weizmann Institute). The authors would like to thank the referees for valuable comments and interesting suggestions which helped in improving the manuscript.

### REFERENCES

- ALUIE, H. & KURIEN, S. 2011 Joint downscale fluxes of energy and potential enstrophy in rotating stratified Boussinesq flows. *Europhys. Lett.* **96** (4), 44006.
- BABIN, A., MAHALOV, A., NICOLAENKO, B. & ZHOU, Y. 1997 On the asymptotic regimes and the strongly stratified limit of rotating Boussinesq equations. *Theor. Comput. Fluid Dyn.* **9**, 223–251.
- BAER, F. & TRIBBIA, J. J. 1977 On complete filtering of gravity modes through nonlinear initialization. *Mon. Weath. Rev.* **105**, 1536–1539.
- BARTELLO, P. 1995 Geostrophic adjustment and inverse cascades in rotating stratified turbulence. *J. Atmos. Sci.* **52**, 4410–4428.
- BARTELLO, P. & TOBIAS, S. M. 2013 Sensitivity of stratified turbulence to the buoyancy Reynolds number. *J. Fluid Mech.* **725**, 1–22.

- BIFERALE, L., MUSACCHIO, S. & TOSCHI, F. 2012 Inverse energy cascade in three-dimensional isotropic turbulence. *Phys. Rev. Lett.* **108** (16), 164501.
- BILLANT, P. & CHOMAZ, J.-M. 2001 Self-similarity of strongly stratified inviscid flows. *Phys. Fluids* **13** (6), 1645–1651.
- BOFFETTA, G. & ECKE, R. E. 2012 Two-dimensional turbulence. *Annu. Rev. Fluid Mech.* **44**, 427–451.
- BRETHOUWER, G., BILLANT, P., LINDBORG, E. & CHOMAZ, J. M. 2007 Scaling analysis and simulation of strongly stratified turbulent flows. *J. Fluid Mech.* **585**, 343–368.
- BRUNNER-SUZUKI, A.-M. E. G., SUNDERMEYER, M. A. & LELONG, M. P. 2014 Upscale energy transfer by the vortical mode and internal waves. *J. Phys. Oceanogr.* **44**, 2446–2469.
- BÜHLER, O., CALLIES, J. & FERRARI, R. 2014 Wave–vortex decomposition of one-dimensional ship-track data. *J. Fluid Mech.* **756**, 1007–1026.
- CALLIES, J., FERRARI, R. & BÜHLER, O. 2014 Transition from geostrophic turbulence to inertia–gravity waves in the atmospheric energy spectrum. *Proc. Natl Acad. Sci. USA* **111** (48), 17033–17038.
- CAMPAGNE, A., GALLET, B., MOISY, F. & CORTET, P.-P. 2015 Disentangling inertial waves from eddy turbulence in a forced rotating-turbulence experiment. *Phys. Rev. E* **91** (4), 043016.
- CELANI, A., MUSACCHIO, S. & VINCENZI, D. 2010 Turbulence in more than two and less than three dimensions. *Phys. Rev. Lett.* **104** (18), 184506.
- CHARNEY, J. G. 1971 Geostrophic turbulence. *J. Atmos. Sci.* **28**, 1087–1094.
- DEUSEBIO, E., BOFFETTA, G., LINDBORG, E. & MUSACCHIO, S. 2014 Dimensional transition in rotating turbulence. *Phys. Rev. E* **90**, 023005.
- DEWAN, E. M. 1979 Stratospheric wave spectra resembling turbulence. *Science* **204**, 832–835.
- EMBID, P. F. & MAJDA, A. J. 1998 Low Froude number limiting dynamics for stably stratified flow with small or finite Rossby numbers. *Geophys. Astrophys. Fluid Dyn.* **87** (1–2), 1–50.
- ERRICO, R. M. 1984 The statistical equilibrium solution of a primitive-equation model. *Tellus A* **36** (1), 42–51.
- FARRELL, B. F. & IOANNOU, P. J. 2009 A theory of baroclinic turbulence. *J. Atmos. Sci.* **66**, 2444–2454.
- FARRELL, B. F. & IOANNOU, P. J. 2012 Dynamics of streamwise rolls and streaks in turbulent wall-bounded shear flow. *J. Fluid Mech.* **708**, 149–196.
- FERRARI, R. & WUNSCH, C. 2009 Ocean circulation kinetic energy: reservoirs, sources, and sinks. *Annu. Rev. Fluid Mech.* **41** (1), 253–282.
- GAGE, K. S. 1979 Evidence for  $k^{-5/3}$  law inertial range in mesoscale two-dimensional turbulence. *J. Atmos. Sci.* **36**, 1950–1954.
- GARRETT, C. & MUNK, W. H. 1979 Internal waves in the ocean. *Annu. Rev. Fluid Mech.* **11** (1), 339–369.
- GODEFERD, F. S. & CAMBON, C. 1994 Detailed investigation of energy transfers in homogeneous stratified turbulence. *Phys. Fluids* **6** (6), 2084–2100.
- GODEFERD, F. S. & STAQUET, C. 2003 Statistical modelling and direct numerical simulations of decaying stably stratified turbulence. Part 2. Large-scale and small-scale anisotropy. *J. Fluid Mech.* **486**, 115–159.
- GODOY-DIANA, R., CHOMAZ, J.-M. & BILLANT, P. 2004 Vertical length scale selection for pancake vortices in strongly stratified viscous fluids. *J. Fluid Mech.* **504**, 229–238.
- HASSELMANN, K. 1966 Feynman diagrams and interaction rules of wave–wave scattering processes. *Rev. Geophys.* **4** (1), 1–32.
- HERBERT, C. 2014 Restricted partition functions and inverse energy cascades in parity symmetry breaking flows. *Phys. Rev. E* **89**, 013010.
- HERBERT, C., POUQUET, A. & MARINO, R. 2014 Restricted equilibrium and the energy cascade in rotating and stratified flows. *J. Fluid Mech.* **758**, 374–406.
- HERRING, J. R. & MÉTAIS, O. 1989 Numerical experiments in forced stably stratified turbulence. *J. Fluid Mech.* **202** (1), 97–115.
- IVEY, G. N., WINTERS, K. B. & KOSEFF, J. R. 2008 Density stratification, turbulence, but how much mixing? *Annu. Rev. Fluid Mech.* **40** (1), 169–184.

- KARTASHOVA, E., NAZARENKO, S. & RUDENKO, O. 2008 Resonant interactions of nonlinear water waves in a finite basin. *Phys. Rev. E* **78**, 016304.
- KIMURA, Y. & HERRING, J. R. 2012 Energy spectra of stably stratified turbulence. *J. Fluid Mech.* **698**, 19–50.
- KITAMURA, Y. & MATSUDA, Y. 2010 Energy cascade processes in rotating stratified turbulence with application to the atmospheric mesoscale. *J. Geophys. Res.* **115**, D11104.
- KRAICHNAN, R. H. 1967 Inertial ranges in two-dimensional turbulence. *Phys. Fluids* **10**, 1417–1423.
- KRAICHNAN, R. H. & MONTGOMERY, D. C. 1980 Two-dimensional turbulence. *Rep. Prog. Phys.* **43**, 547.
- KURIEN, S. & SMITH, L. M. 2012 Asymptotics of unit Burger number rotating and stratified flows for small aspect ratio. *Physica D* **241** (3), 149–163.
- KURIEN, S. & SMITH, L. M. 2014 Effect of rotation and domain aspect-ratio on layer formation in strongly stratified Boussinesq flows. *J. Turbul.* **15** (4), 241–271.
- LAVAL, J.-P., MCWILLIAMS, J. C. & DUBRULLE, B. 2003 Forced stratified turbulence: successive transitions with Reynolds number. *Phys. Rev. E* **68** (3), 036308.
- LEE, T. D. 1952 On some statistical properties of hydrodynamical and magneto-hydrodynamical fields. *Q. Appl. Maths* **10**, 69–74.
- LEITH, C. E. 1980 Nonlinear normal mode initialization and quasi-geostrophic theory. *J. Atmos. Sci.* **37**, 958–968.
- CLARK DI LEONI, P. & MININNI, P. D. 2015 Absorption of waves by large-scale winds in stratified turbulence. *Phys. Rev. E* **91** (3), 033015.
- LIEN, R.-C. & MÜLLER, P. 1992 Consistency relations for gravity and vortical modes in the ocean. *Deep-Sea Res.* **39** (9), 1595–1612.
- LILLY, D. K. 1983 Stratified turbulence and the mesoscale variability of the atmosphere. *J. Atmos. Sci.* **40**, 749–761.
- LILLY, D. K., BASSETT, G., DROEGEMEIER, K. & BARTELLO, P. 1998 Stratified turbulence in the atmospheric mesoscales. *Theor. Comput. Fluid Dyn.* **11** (3–4), 139–153.
- LINDBORG, E. 2005 The effect of rotation on the mesoscale energy cascade in the free atmosphere. *Geophys. Res. Lett.* **32** (1), L01809.
- LINDBORG, E. 2006 The energy cascade in a strongly stratified fluid. *J. Fluid Mech.* **550**, 207–242.
- LINDBORG, E. 2015 A Helmholtz decomposition of structure functions and spectra calculated from aircraft data. *J. Fluid Mech.* **762**, R4.
- LONGUET-HIGGINS, M. S., GILL, A. E. & KENYON, K. 1967 Resonant interactions between planetary waves. *Proc. R. Soc. Lond. A* **299**, 120–144.
- MARINO, R., MININNI, P. D., ROSENBERG, D. & POUQUET, A. 2013 Inverse cascades in rotating stratified turbulence: fast growth of large scales. *Europhys. Lett.* **102**, 44006.
- MARINO, R., MININNI, P. D., ROSENBERG, D. L. & POUQUET, A. 2014 Large-scale anisotropy in stably stratified rotating flows. *Phys. Rev. E* **90** (2), 023018.
- MARINO, R., POUQUET, A. & ROSENBERG, D. 2015 Resolving the paradox of oceanic large-scale balance and small-scale mixing. *Phys. Rev. Lett.* **114**, 114504.
- MCKEON, B. J. & SHARMA, A. S. 2010 A critical-layer framework for turbulent pipe flow. *J. Fluid Mech.* **658**, 336–382.
- MÉTAIS, O., BARTELLO, P., GARNIER, E., RILEY, J. J. & LESIEUR, M. 1996 Inverse cascade in stably stratified rotating turbulence. *Dyn. Atmos. Oceans* **23** (1), 193–203.
- MÉTAIS, O., RILEY, J. J. & LESIEUR, M. 1994 Numerical simulations of stably-stratified rotating turbulence. In *Stably-Stratified Flows – Flow and Dispersion over Topography* (ed. I. P. Castro & N. J. Rockliff), pp. 139–151. Oxford University Press.
- MININNI, P. D. 2011 Scale interactions in magnetohydrodynamic turbulence. *Annu. Rev. Fluid Mech.* **43** (1), 377–397.
- MININNI, P. D., ROSENBERG, D. & POUQUET, A. 2012 Isotropization at small scales of rotating helically driven turbulence. *J. Fluid Mech.* **699**, 263–279.
- MININNI, P. D., ROSENBERG, D., REDDY, R. & POUQUET, A. 2011 A hybrid MPI–OpenMP scheme for scalable parallel pseudospectral computations for fluid turbulence. *Parallel Comput.* **37**, 316–326.

- MOARREF, R. & JOVANOVIĆ, M. R. 2010 Controlling the onset of turbulence by streamwise travelling waves. Part 1. Receptivity analysis. *J. Fluid Mech.* **663**, 70–99.
- MÜLLER, P., HOLLOWAY, G., HENYEY, F. & POMPHREY, N. 1986 Nonlinear-interactions among internal gravity-waves. *Rev. Geophys.* **24** (3), 493–536.
- NASTROM, G. D., GAGE, K. S. & JASPERSON, W. H. 1984 Kinetic energy spectrum of large-and mesoscale atmospheric processes. *Nature* **310**, 36–38.
- NAZARENKO, S. V. 2010 *Wave Turbulence*, Lecture Notes in Physics, vol. 825. Springer.
- NEWELL, A. C. 1969 Rossby wave packet interactions. *J. Fluid Mech.* **35**, 255–271.
- NEWELL, A. C. & RUMPF, B. 2011 Wave turbulence. *Annu. Rev. Fluid Mech.* **43** (1), 59–78.
- POUQUET, A. & MARINO, R. 2013 Geophysical turbulence and the duality of the energy flow across scales. *Phys. Rev. Lett.* **111**, 234501.
- POUQUET, A., SEN, A., ROSENBERG, D., MININNI, P. & BAERENZUNG, J. 2013 Inverse cascades in turbulence and the case of rotating flows. *Phys. Scr. T* **155**, 014032.
- PRAUD, O., FINCHAM, A. M. & SOMMERIA, J. 2005 Decaying grid turbulence in a strongly stratified fluid. *J. Fluid Mech.* **522**, 1–33.
- RILEY, J. J. & DE BRUYN KOPS, S. M. 2003 Dynamics of turbulence strongly influenced by buoyancy. *Phys. Fluids* **15**, 2047–2059.
- RILEY, J. J. & LELONG, M.-P. 2000 Fluid motions in the presence of strong stable stratification. *Annu. Rev. Fluid Mech.* **32** (1), 613–657.
- RILEY, J. J., METCALFE, R. W. & WEISSMAN, M. A. 1981 Direct numerical simulations of homogeneous turbulence in density-stratified fluids. In *AIP Conf. Proc.*, vol. 76, pp. 79–112. American Institute of Physics.
- RORAI, C., MININNI, P. D. & POUQUET, A. 2014 Turbulence comes in bursts in stably stratified flows. *Phys. Rev. E* **89**, 043002.
- ROSENBERG, D., POUQUET, A., MARINO, R. & MININNI, P. D. 2015 Evidence for Bolgiano–Obukhov scaling in rotating stratified turbulence using high-resolution direct numerical simulations. *Phys. Fluids* **27**, 055105.
- SAGAUT, P. & CAMBON, C. 2008 *Homogeneous Turbulence Dynamics*. Cambridge University Press.
- SAHOO, G., BONACCORSO, F. & BIFERALE, L. 2015 On the role of helicity for large-and small-scales turbulent fluctuations. *Phys. Rev. E* **92** (5), 051002.
- SHARMA, A. S. & MCKEON, B. J. 2013 On coherent structure in wall turbulence. *J. Fluid Mech.* **728**, 196–238.
- SMITH, L. M., CHASNOV, J. R. & WALEFFE, F. 1996 Crossover from two- to three-dimensional turbulence. *Phys. Rev. Lett.* **77** (12), 2467–2470.
- SMITH, L. M. & WALEFFE, F. 2002 Generation of slow large scales in forced rotating stratified turbulence. *J. Fluid Mech.* **451**, 145–168.
- SMYTH, W. D. & MOUM, J. N. 2000a Anisotropy of turbulence in stably stratified mixing layers. *Phys. Fluids* **12** (6), 1343–1362.
- SMYTH, W. D. & MOUM, J. N. 2000b Length scales of turbulence in stably stratified mixing layers. *Phys. Fluids* **12** (6), 1327–1342.
- SOZZA, A., BOFFETTA, G., MURATORE-GINANNESCHI, P. & MUSACCHIO, S. 2015 Dimensional transition of energy cascades in stably stratified forced thin fluid layers. *Phys. Fluids* **27**, 035112.
- STAQUET, C. & GODEFERD, F. S. 1998 Statistical modelling and direct numerical simulations of decaying stably stratified turbulence. Part 1. Flow energetics. *J. Fluid Mech.* **360**, 295–340.
- STAQUET, C. & SOMMERIA, J. 2002 Internal gravity waves: from instabilities to turbulence. *Annu. Rev. Fluid Mech.* **34** (1), 559–593.
- SUKHATME, J. & SMITH, L. M. 2008 Vortical and wave modes in 3D rotating stratified flows: random large-scale forcing. *Geophys. Astrophys. Fluid Dyn.* **102** (5), 437–455.
- VALLIS, G. K. 2006 *Atmospheric and Oceanic Fluid Dynamics: Fundamentals and Large-scale Circulation*. Cambridge University Press.
- VANNESTE, J. 2013 Balance and spontaneous wave generation in geophysical flows. *Annu. Rev. Fluid Mech.* **45**, 147–172.
- WAITE, M. L. 2013 Potential enstrophy in stratified turbulence. *J. Fluid Mech.* **722**, R4.

- WAITE, M. L. & BARTELLO, P. 2004 Stratified turbulence dominated by vortical motion. *J. Fluid Mech.* **517**, 281–308.
- WAITE, M. L. & BARTELLO, P. 2006a Stratified turbulence generated by internal gravity waves. *J. Fluid Mech.* **546**, 313–339.
- WAITE, M. L. & BARTELLO, P. 2006b The transition from geostrophic to stratified turbulence. *J. Fluid Mech.* **568**, 89–108.
- WARN, T. 1986 Statistical mechanical equilibria of the shallow water equations. *Tellus A* **38** (1), 1–11.
- WARN, T., BOKHOVE, O., SHEPHERD, T. G. & VALLIS, G. K. 1995 Rossby number expansions, slaving principles, and balance dynamics. *Q. J. R. Meteorol. Soc.* **121** (523), 723–739.
- WHITEHEAD, J. P. & WINGATE, B. A. 2014 The influence of fast waves and fluctuations on the evolution of the dynamics on the slow manifold. *J. Fluid Mech.* **757**, 155–178.
- ZAKHAROV, V. E., LVOV, V. S. & FALKOVICH, G. 1992 *Kolmogorov Spectra of Turbulence*. Springer.
- ZEMAN, O. 1994 A note on the spectra and decay of rotating homogeneous turbulence. *Phys. Fluids* **6**, 3221–3223.
- ZHU, J.-Z., YANG, W. & ZHU, G.-Y. 2014 On one-chiral-sector-dominated turbulence states. *J. Fluid Mech.* **739**, 479–501.